Carbon-dioxide degassing of geothermal fluids

Experimental Research using corefloods and CT scanning

AESB3400: Bachelor End Project

Anushka Tripathi

Delft University of Technology

TU Delft

Carbon-dioxide degassing of geothermal fluids

Experimental Research using corefloods and CT scanning

by

Anushka Tripathi

Student Name	Student Number
Anushka Tripathi	5001919

Supervisor:	Dr. Pacelli Zitha
Supervisor:	Anne Pluymakers
Project Duration:	May 16, 2022 - July 6th, 2022
Faculty:	Faculty of Civil Engineering and Geoscience, Delft

Cover:	The cover photo is taken from (Ornelas, 2012)
Style:	TU Delft Report Style, with modifications by Daan Zwaneveld

TU Delft

Preface

This report has been made in order to summarise and present the results and conclusions of CT assisted core-flood experiments for carbon-dioxide degassing of geothermal fluids. The experimental analysis spanned a period of 2 months as part of the Bachelor's End Project. First, I would like to thank to Dr. Pacelli Zitha for allowing me to pursue this research topic. Next, I would like to thank Dr. Chris Boeije for supervising and helping me throughout the duration of the project. I would also like to thank Dr. Sian Jones for helping me in preparing the core for the experiments. I would also like to thank Ellen Meijvogel-dekoning for scanning the core. Last but not the least I would like to thank Michiel Slob for setting up the core-flood set up without which the experiments would have not been carried out.

Anushka Tripathi
Delft, July 2022

Abstract

Global energy transition is crucial in mitigating climate change. Numerous initiatives are being taken globally to achieve a carbon-neutral energy system. These goals require a complete shift from non-renewable energy sources to renewable sources like geothermal energy. These renewable sources of energy have to be constantly improved in order to maximise their efficiency and to ensure the cleanest possible source of energy. One of the challenges in geothermal energy is degassing of geothermal fluids. These fluids contain a lot of minerals and chemicals dissolved in them that are at equilibrium at a certain pressure and temperature. When there is change in this pressure and temperature during extraction, the equilibrium condition changes and the gases dissolved in the fluids degas. These gases then get trapped in pores and decrease the efficiency of extraction of these fluids. They might also prove harmful to the environment due to release of greenhouse gases from the geothermal fluids. The aim of this experimental research project is to visualise the degassing of geothermal fluids and understand the conditions and affect of degassing on the core.

The experiments were carried out by injecting either tap water or brine at a set flow rate of 15ml/min and different concentrations of CO_2. Each experiment had a specific concentration of CO_2 which was injected simultaneously with brine at a certain back-pressure. Then the back-pressure was lowered gradually and when the fluid de-gassed it was allowed to reach steady state and a scan of the core was taken. Throughout the experiments pressure measurements were taken along the core.

There was a decrease in overall permeability of the core by a factor of 2 after the end of the experiments.The outlet of the core also experienced a decrease in permeability by a factor of 3. The permeability values just after the switching tap water with brine were already lower. The overall decrease at the end of the experiments could be explained by calcite precipitation due to reaction of CO_2 with calcium carbonate present in the brine injected. There was also a significant decrease in porosity values near the inlet of the core which could be due to presence of contaminants in tap water/brine injected. The degassing of the fluid injected with lower concentration of CO_2 seem to follow Henry's law with however an offset of 4 bars. This is explained by formation of carbonic acid or changes in pH and also overshooting of gases by mass flow controller. The lower salinity experiments of 0.2 mol/L follows the model by Duan and Sun. A plot of effective permeability versus pressure drop was also made which shows a four times less effective permeability for high salinity experiments. Saturation maps were made by utilising the scans made by the CT scan of the core. The saturation map of lower concentration show a clear gas front as the back-pressure is lowered. The higher concentrations show a gravity segregation effect due to difference in density. Finally, a lot of pressure drop versus saturation values was made which shows a greater pressure drop for the higher salinity experiments.

Contents

1

Introduction

In recent times there have been numerous initiatives being taken globally to transition from non-renewable to clean renewable energy sources. The Paris Agreement of 2015 concluded with the United Nations for Climate Change agreeing on the urgent need to minimise increase in mean global temperature. According to the IRENA's World Energy's Transition outlook, the ongoing pace of the energy transition is not enough to tackle the global greenhouse gas emissions in order to achieve the ambitious goals set out globally. If the current pace continues then the carbon emissions from energy sources will only increase and are predicted to be 6 % more than 2015 (Gielen et al., 2019). Research indicates that within the Netherlands itself a six fold increase in the the pace of transition is required to be able to achieve long term sustainability goals (EBN , DAGO, Mckinsey Company, & Stichting Platform Geothermie, 2019). It requires new innovations in all fronts of the energy sector to push the global energy industry away from fossil fuels and eventually making the world carbon neutral(IRENA , 2022).

Renewable energy sources are the key drivers of this transition accounting to 94 % in emission reductions(Gielen et al., 2019). Geothermal energy is one of these renewable energy sources having the potential to lead to carbon neutral energy systems. It is a clean and sustainable alternative for a variety of applications mainly spatial heating and electricity generation. In order to meet the national and global energy demand and to transition towards sustainable energy systems worldwide the efficiency of renewable energy sources have to be increased.

There are a variety of challenges present, one of them being degassing of geothermal fluids. Geothermal fluids contain a plethora of dissolved minerals and gases. In order to extract these fluids from the subsurface there is a decrease in pressure near the well head which also results in changes in the equilibrium of the dissolved matter and eventual release of dissolved gases such as carbon dioxide. Due to the presence of these exsolved gases there is an overall decrease in the efficiency of the process. This decrease in efficiency occurs due to the dual phase fluid flowing into the heat exchangers (Chabab et al., 2021). This results in a decrease in efficiency of heat transfer since the fluid is no longer single phase. The gases also alter the pH levels of the fluids thus resulting in other issues such as calcium carbonate scaling in the walls of the pipes. These released gases also get trapped in the pores of the aquifer resulting in a reduction of hydraulic conductivity of the medium. These brines also contain gases such as methane and carbon-dioxide resulting in a potential danger of emission of greenhouse gases in the atmosphere (Chabab et al., 2021).

The aim of this project is to visualise and understand under what conditions degassing of geothermal fluids occurs by conducting a series of core-flood experiments on a Berea core via simultaneous injection of tap water and or brine along with carbon-dioxide. The coreflood experiments also involve taking a CT scan of the core once a certain steady state is reached in order to create saturation maps of the bubbles degassed from the fluid.

2

Theoretical Background

This chapter gives a brief overview of flow in the subsurface, geothermal fluids, solubility of gases in fluids, and finally an overview of CT scan analysis.

2.1. Fluid flow (Darcy's Law)

Darcy's law is the governing law that describes the flow of fluids in porous media. This law is discussed in order to be able to understand the effect of degassing on the permeability of the rock. The law was formulated by obtaining the results of experimental research on flow of water through sand. The law for one dimensional flow is stated as follows

$$\frac{Q}{A} = -K_s \frac{dh}{ds} = q \tag{2.1}$$

Where A is the area of cross section in (m^2), q is the flow rate in (m/s) also called darcy velocity, Q is the volumteric flow rate in (m^3/s), K_s is the hydraulic conductivity of the porous medium in the direction of flow in (m/s), dh is the hydraulic gradient and s is the direction of the flow. The hydraulic conductivity in the equation accounts for the ease of flow through the porous media and is property of the medium. In order to account for the property of fluid flowing through the medium intrinsic permeability is often used. The intrinsic permeability is related to hydraulic conductivity as presented in equation 2.2 below(Fitts, 2013).

$$k = \frac{K\mu}{\rho g} \tag{2.2}$$

Where k is the intrinsic permeability, μ is dynamic viscosity of the fluid flowing, $\rho$is the density of the fluid and g is the acceleration due to gravity. The SI unit for permeability as described above is m^2, however in subsurface applications it is described by the unit Darcy. The relation between Darcy and cm^2 is described below(Fitts, 2013).

$$1Darcy \approx 10^{-12} m^2 \tag{2.3}$$

The hydraulic gradient is the reason for the flow of the fluid since fluid flows from higher hydraulic head to lower hydraulic head. In order to account for constant elevation the Darcy's law is stated as follows ;

$$\frac{Q}{A} = \frac{k}{\mu} \frac{\Delta P}{L} = q \tag{2.4}$$

Where ΔP is the pressure drop over the medium in (Pa) at a distance L in (m)(Atangana, 2018).

Since the experiment involves degassing of geothermal fluids, multi phase fluid flow would occur instead of a single phase. The degassed bubbles will affect the flow of water through the rock. In order to asses this effective permeability is described as follows (Verweij, 2021)

$$k_{eff} = \frac{q}{\Delta(P)}\mu L \tag{2.5}$$

In order to ensure the validity of Darcy's law for the fluid flow through porous media, the flow has to be laminar. Reynold's number determines whether the flow of the fluid is laminar or turbulent. The Reynold's number for flow through porous media is defined as follows

$$Re = \frac{\rho D_p q}{\mu} \tag{2.6}$$

Where Re is the Reynold's number, D_p is the pore diameter for the porous media, q is the fluid velocity, ρ is the density of the media and μ is the dynamic viscosity of the fluid flowing(Fitts, 2013). The critical Reynold's number varies depending on the type of media the fluid is flowing through. The values for these media differ per study and research. The range for disordered porous media is 0.01 - 0.1. The range for loosely consolidated sand bed is 0.4 - 3 and for consolidated material is 10 - 1000. A widespread agreement among researchers is a range of 1-10 for porous media depending on average grain size and velocity(Wang, Li, Zhao, Chen, & Xu, 2019). The corelfood experiments were performed using a flow rate of 15 ml/min on a Berea core. Berea sandstones usually have a pore radius of around 20 micrometeres. They have a particle diameter of around 185 micrometer(Wetzel, Kempka, & Kühn, 2021). Using these properties the Reynold's number for the flow rate used in the experiments was calculated to be 0.209. Thus the flow rate used satisfies the condition of laminar flow and Darcy's law for flow is applicable.

2.2. Composition of geothermal fluids

Geothermal fluids are the fluids extracted from a geothermal reservoir and then is usually redirected to a power plant. Geothermal fluids vary a lot in chemical composition depending on the location of the geothermal reservoir and the composition in the same reservoir can change over time. According to the Argonne Geothermal Geochemical Database (AGGD) the most common chemicals found in geothermal fluids are sodium(Na), chloride(Cl), bicarbonate(HCO_3), sulphate(SO_4^2-), silica(SiO_2), pottasium(Ka) and calcium(Ca) (Finster, Clark, Schroeder, & Martino, 2015).

Similarly the geothermal fluids also contain a variety of dissolved gases such as carbon-dioxide, nitrogen, hydrogen sulphide, hydrogen and methane. H2O-NaCl-CO2 is the most characteristic ternary composition of geothermal fluid. The phrase CO2 refers to the effect of non-condensable gases, whereas NaCl in the mixture refers to the total salts in reservoir fluid (Flores, Meza, L., & Aragón, 2017). The average CO_2 concentration in geothermal reservoirs is usually between 114 mmol/L to 227 mmol/L, however in Western Turkey much higher concentrations between 340 mmol/L to 772 mmol/L have been reported(Haizlip, Stover, Garg, Tut Haklidir, & Prina, 2016). In order to quantify the salinity of the geofluids the term TDS or total dissolved solids is used since commonly the solids and ions dissolved these fluids are salts. The most common dissolved salt in geothermal fluids is sodium chloride(NaCl)(Fitts, 2013). In Germany in the Gros Schonenbeck geothermal well the concentration of the dissolved salts was reported to be around 265 g/L (Blöcher et al., 2016).

2.3. Gas solubility

The solubility of gases in liquids is explained by Henry's law which states that the solubility of the gas is proportional to the partial pressure of the gas. At standard temperature of 298.15 K the proportionality factor of the gas phase is described by Henry's law constant. This is described in the formula below (Sander, 2015)

$$H^{cp} = \frac{Ca}{p} \tag{2.7}$$

Where C_a is the concentration of the gas in mol/L, p is the pressure of the gas in atm and H^{cp} is in mol/m^3Pa. The above described equation is only valid for 298.15 K, for other temperatures the Van't Hoff equation is used to describe the Henry's law constant. In general as temperature increases the amount of gas that can be dissolved decreases. This equation has been described below (Sander, 2015)

$$H(T) = H°exp[\frac{-\Delta_{sol}H}{R}(\frac{1}{T} - \frac{1}{T°})] \tag{2.8}$$

Where H(T) is the Henry's constant at the desired temperature, H is the Henry's law constant at 298.15°K, $\Delta_{sol}H$ describes the dissolution enthalpy. Using this equation the Henry's laws constants for different temperatures have been derived. Since the experiments will be carried out in the CT scan room, which is colder than room temperature, the solubility of CO_2 has been calculated for measured temperature of 18°C along with other temperatures and presented in the plot 2.1 below.

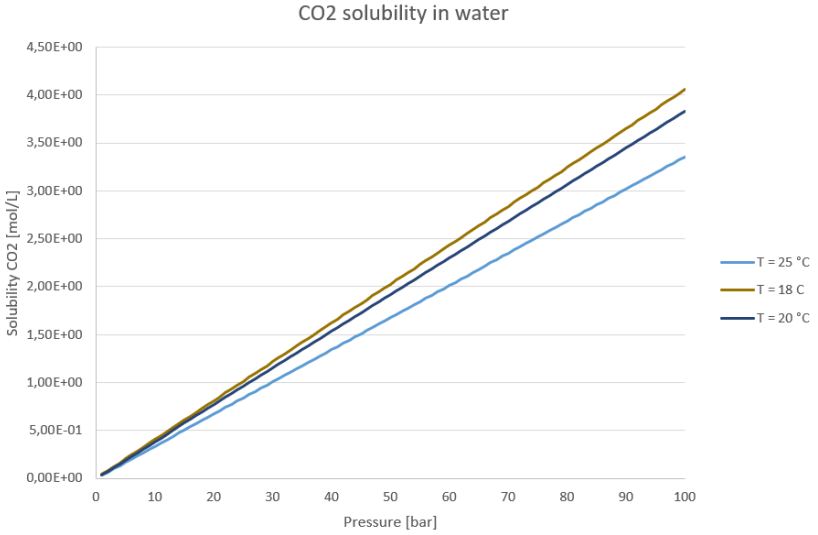

Figure 2.1: Henry's law for different temperatures for CO_2

The solubility of gases in salt solutions is less than that in pure water. This effect is called "salting out" and is due to the increase in ionic strength of the fluid in which the gas is being dissolved (Hermann, Dewes, & Schumpe, 1995). An article by Duan and Sun presents a model of solubility of carbon-dioxide in water and in NaCl solutions in temperatures ranging from 273 K to 533 K and pressure ranging between 0 to 2000 bars. This model is based on the equation of state by Duan and Sun that is based on specific particle interaction theory(Duan & Sun, 2003). From this model a contour plot was generated for the 1 M NaCl brine used in the experiments, which presents iso-solubility contour lines as a function temperature and pressure. This plot is later used to compare the results of the low salinity experiments with the model.

2.4. Gas trapping in pores

In general when the degassing of geothermal fluids occur, the bubbles formed as a result can either travel upwards in the subsurface due to bouyant forces however the bigger bubbles get trapped in the pore spaces in the sediments. These trapped gas bubbles can result in significant decrease of hydraulic conductivity of the porous medium(Mahabadi, Zheng, Yun, van Paassen, & Jang, 2018).

The behaviour of gas bubbles in the subsurface such as getting trapped in pores or migration depends on the size of the bubbles formed, the bubbles joining together, the rate at which the bubbles are forming and growing and also on pore scale characteristics of the medium. As the bubbles move forward through the pores they can also join together forming bigger bubbles and therefore get trapped if the size of the resulting bubbles is larger than the pore throat diameter. The pore size characteristics and distribution of the porous medium significantly affect the size characteristics of the gas bubbles formed from degassing of carbon-dioxide rich water and these bubbles formed are uniformly distributed throughout the medium(Zuo & Benson, 2014). The gas bubbles also get held back by the capillary forces acting on a pore scale level and these forces prevent the bubbles from migrating upwards through the aquifer or the reservoir (Wildenschild, Armstrong, Herring, Young, & William Carey, 2011).

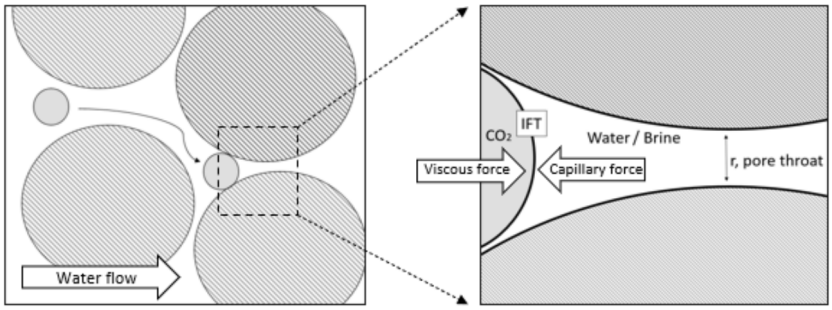

Figure 2.2: (Right) Bubble moving through pores and getting trapped, (left) Forces acting on trapped bubble (Verweij, 2021)

The left side of Figure 2.2 illustrates gas bubbles moving through pores and due to one of the bubbles being larger than the pore throat size, it gets trapped in between the pores. The right side describes the various forces acting on a pore scale level at the bubbles trapped between the pores.

2.5. Saturation and Porosity Mapping

In order to visualise how the degassed carbon-dioxide bubbles saturate the core depending on the pressure changes, a medical CT scanner is used to scan the core-holder once steady state has been achieved after the degassing has occurred. The core-holder was also scanned before the start of the core-holder to get a dry scan of the core which will be utilised to generate the porosity and the saturation maps. The porosity map for the core is obtained using Equation 2.9 presented below (Benson, Perrin, Krause, Kuo, & Miljković, 2008).

$$\phi = \frac{CT^{sat}_{brine} - CT_{dry}}{CT_{brine} - CT_{air}} \tag{2.9}$$

Where CT^{sat}_{brine} refers to the scan of the brine saturated core and CT_{dry} refers to the scan of the dry core. The console converts the X-ray attenuation coefficients into numbers referred to as CT number. These numbers come from a linear density scale referred to as "Hounsfields Units", HU. According to this scale de-ionized water is assigned a value of 0. For the core-foods tap water was used and its CT value is taken to be same as de-ionized water and that of air is taken to be -1000. (Lev & Gonzalez, 2002) The saturation maps utilise three sets of scans: brine saturated images, dry scan, and experimental images in steady state. The equation used to obtain the saturation is presented below (Benson et al., 2008).

$$S_{CO_2} = \frac{CT_{exp} - CT^{sat}_{brine}}{CT_{dry} - CT^{sat}_{brine}} \tag{2.10}$$

3

Methodology

In the coreflood experiments, CO2 was coinjected with either tap water or a 1M NaCl brine solution in the berea core and then CT scans were done. In this chapter the methodology of the experiments conducted would be discussed. The first section describes the experimental setup, the materials used and then the procedure of the experiments will be laid out.

3.1. Experimental setup

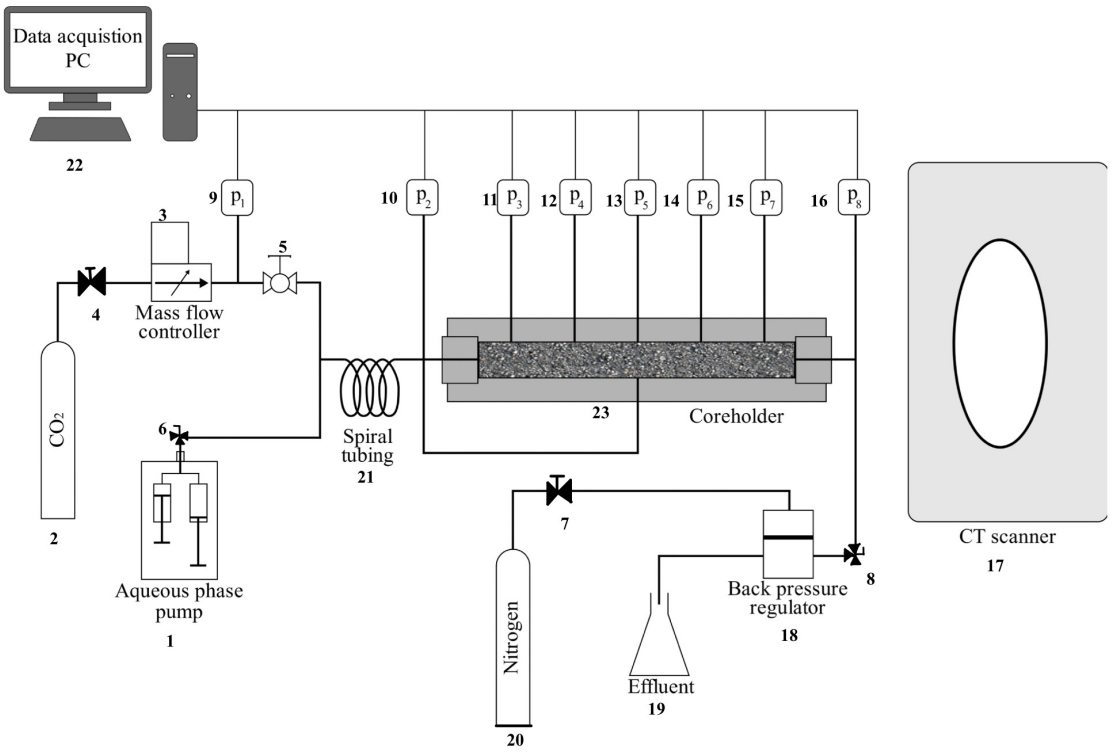

schematic overview of experimental set-up 1 : Aqueous Phase Pump, 2: CO_2 cylinder, 3: Mass flow controller, 4/5/6/7/8: valves, 9-16: pressure transducers, 17: CT scanner, 18: Back pressure regulator, 19: Effluent tank, 20: Nitrogen tank, 21: spiral tubing, 22: computer, 23 : core holder

Figure 3.1: Experimental Setup

Figure 3.1 presents the detailed schematics of the experimental setup in which a series of coreflood experiments were conducted. These experiments were performed on a Berea core, which was placed horizontally on the coreholder. The coreholder consists of polyether ether ketone with the inlet at the left side and an outlet at the right side. The Berea core used for the experiments has a length of 39 cm and a diameter of 4 cm. Along the side of the core, five drill holes were drilled to put in the pressure taps to be able to measure the pressure. The confining pressure on the core was same as the inlet pressure for the coreloods. A dual piston aqueous phase pump (Quizix QX-1500)(1) was used to inject the aqueous phase fluids in the core with a flow rate of 15ml/min. In order to regulate the gas concentrations injected in the core, a mass flow controller(3)(Bronkhorst-EL FLOW) was used which has a range from 1 to 200 g/hour. A series of eight pressure transducers (9-16) (Keller PA33X) were placed along the sides of the core of which 5 were placed equidistant on the core, and the rest on the sides of the core. The pressure transducers were connected to a computer (22) on which the pressure was observed during the experiments and it recorded the data from them every 2 seconds. The pressure transducer (16) present near the outlet of core was used to maintain the back-pressure using a back-pressure regulator (18) which was connected to a nitrogen tank(20). The coreholder is placed in the Seimens SOMATOM Definition CT scan in order to be able to scan the core after every set period of time.

3.2. Materials Used

In this research experiment the corefloods were conducted on a Berea sandstone core of 39 cm length and 4 cm diameter.

Berea sandstones are the sandstones from the Devonian period with medium to fine grains(Pepper, de Witt, & Demarest, 1954). It has a wide range of characteristics, with porosity ranging from 13 to 22 percent and permeability ranging from 50 to 1000 mD. The mineral makeup of the Berea sandstone varies, although it primarily comprises of quartz (80.90 wt), feldspars (45 wt), and clay minerals (28 wt)(Dawson, Pearce, Biddle, & Golding, 2015).

Tap water was used for the first sets of core flood studies. To avoid clay particles from dissolving from the cores, tap water was utilized instead of demineralized water. A 1 mol/L $NaCl$ solution was used in the last batch of core flood experiments. The brine solution was made by dissolving 58.44 grams of NaCl in demineralized water and then it was degassed. The high salinity experiments were performed by using 1.5 mol/L $CaCl_2$ and 2 mol/L $NaCl$ solution which is equivalent to 283.35 g/L of dissolved salts.

3.3. Experimental Methodology

The procedure for the various experiments will be detailed in this section. A permeability test has been performed on the core to precisely assess its permeability. A number of CT scan assisted corefloods were carried out to determine when the degassing process began and what effect it had on the saturation of cores with bubbles.

3.3.1. Permeability Test

In order to estimate the permeability of the core, tap water was injected with different flow rates for a set period of time and the pressure drop measured along the core was recorded. The flow rates used were 5, 10, 15, 20, 25 and 30 ml/min. The flow rate was set using the phase pump and then once steady state had been achieved, the flow rate was changed and the process was repeated. The permeability test was carried out before the start of the core-floods and once when all the core-flood experiments have been completed.

In order to calculate the value of permeability from the pressure data recorded from the tests, a plot of flow rates (Q/A) and pressure drop gradient ($\Delta P/\mu L$) was made. The slope of the plot is the permeability value. When the plot is made the flow rates have to be on a straight line to confirm a laminar flow regime and validity of Darcy's law.

3.3.2. Porosity Measurement

In order to create the porosity map for the core being used for the core-floods, a dry scan of the core was taken before the start of the experiments. Once the core had been saturated with tap water, a wet scan was then taken. Then using Equation 2.9 by normalising the scans for the linear coefficient of water, the porosity map of the core was obtained. This procedure repeated again after the end of the core-floods in order to observe the changes occurred in the core due to the core-floods.

3.3.3. Core-flood Experiments

In order to visualise and understand the saturation of core with gas due to degassing of tap water and or brine, a series of CT scan assisted core-flood experiments were carried out on a 39 cm Berea core. The experiments involved injecting tap water and or brine into the core at a constant flow rate of 15 ml/min. The core was simultaneously injected with a constant concentration of CO_2. Each experiment was carried out at different back pressures and it was lowered throughout the experiment once steady state was achieved. The degassing pressure for a given concentration of CO_2 was estimated using Henry's Law and at the start of the core-floods the back pressure was kept higher than that pressure. The back pressure was then subsequently lowered after steady state, once this pressure was closer to expected degassing pressure it was lowered gradually till degassing was observed. Once the steady state is achieved after degassing,the core was scanned and then back pressure was lowered again. The different concentrations of CO_2, the back pressures and concentration of brine injected per experiment has been summarised in the table 3.1.

Table 3.1: Different parameters used for experiment.

Experiment No.	Water/Brine	CO_2 concentration [mol/L]	Flow rate [ml/min]	Backpressure start [bar]
1	Tap Water	0.3	15	17
2	Tap Water	0.5	15	21
3	Tap Water	0.7	15	27
4	Tap Water	0.9	15	32
5	Tap Water	1.1	15	35
6	Tap Water	1.3	15	43
7	1 M NaCl	0.2	15	15
8	1 M NaCl	0.6	15	27
9	2 M NaCl + 1.5 M $CaCl_2$	0.2	15	25
10	2 M NaCl + 1.5 M $CaCl_2$	0.4	10	25

After the end of each experiment the back-pressure was lowered and then subsequently increased which first resulted in expansion of the gases released and the increased pressure results leads to more solubility and in this way the gases are flushed out of the core.

The degassing starts at the outlet when the back pressure is closer to the pressure at which degassing is expected to occur. Then the degassing process occurs at the next section once the pressure at the region lowers down to the degassing pressure. The sudden rise in the pressure drop shows the start of degassing. When high salinity brine with CO_2 concentration of 0.4 mol/L was injected at a back pressure of 25 bars, the safety limits of the aqueous phase pump was reached. This could be because the brine is more viscous than tap water and lower salinity brine which leads to more pressure drop in the system. The second reason might be the decrease in permeability of the core due to calcium carbonate precipitation. Therefore the flow rate had to be decreased to 10 ml/min in order to be below the safety limits of the pump.

4

Results

In this chapter the results of the permeability and porosity tests and the core-flood experiments have been presented and discussed.

4.1. Permeability tests

Three permeability tests were carried out, one before the start of the core-floods, second one after the tap water was changed to brine and once after the end of all the core-floods.The plot of flow rates versus pressure gradient for the first permeability test have been presented below. The plot 4.1 (top) is the permeability test result for the start of the experiment of the whole core and the straight line indicates a linear relation between flow rates and pressure gradient indicating Darcy's law is valid.

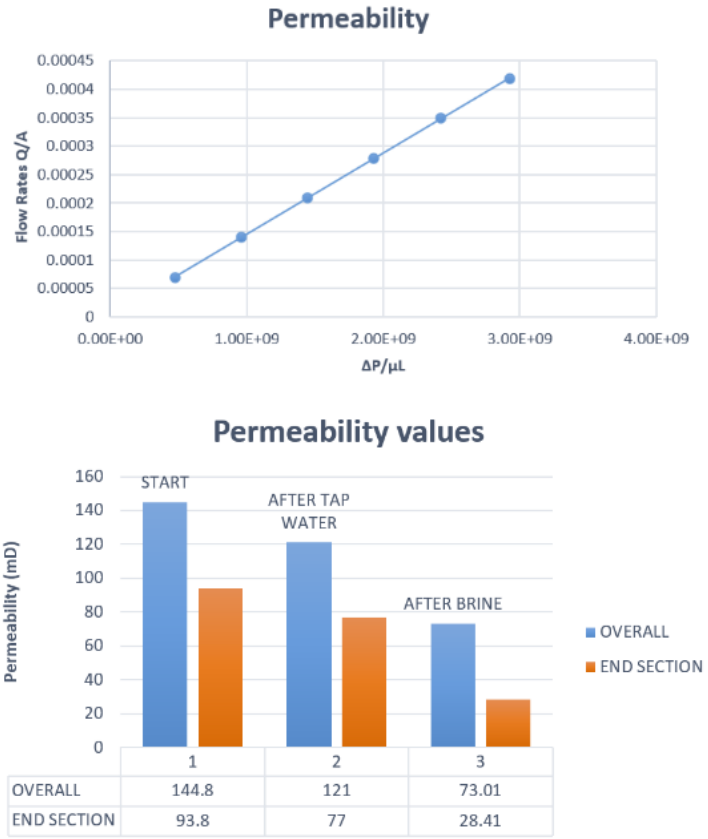

Figure 4.1: (Top) Permeability at the start (Bottom) Permeability values for the whole core and end section

Figure 4.1 shows the permeability values for all the tests for the whole core and the end section. This plot indicates the permeability of the entire core has reduced by a factor of 2 by the end of the experiments and that of end section by a factor of 3. There is however also a decrease in permeability just after switching tap water with brine. The reduction in permeability could be due to a variety of reasons. The most prominent one being calcium carbonate precipitation in the core since the last set of experiments were performed by injecting high salinity brine containing 1.5 M $CaCl_2$ which reacts with CO_2 to form calcium carbonate. The pressure dissipation is highest near the outlet and therefore the degassing of the brine/tap water starts there. This means a lot of CO_2 has exsolved at the outlet throughout the experiments. Therefore, its most susceptible to calcite precipitation due to usage of high salinity brine.

4.2. Pressure Measurements

In order to measure the pressure drop during degassing and also to obtain the permeability of the core 5 pressure taps were put in at the side of the core, and 3 more at the outlet and inlet of the core. The pressure measurements allow to identify the start of degassing of the fluid being injected. When the pressure drop starts rising, it shows that the fluid has degassed and the pressure drop has to be increased to maintain the flow rate.

The pressure measurements of the core-flood experiment with a carbon-dioxide concentration of 0.9 mol/L has been displayed in plot 4.2 below. Pressure tap 8 is present at the outlet of the core. The pressure at the outlet is controlled by changing the back pressure. The experiment was started with a back-pressure of 32 bar. It was lowered to 25 bars at 2000 seconds and then to 22.5 bars at 3000 seconds. With each step of lowering the back-pressure, the system was allowed to reach steady state and then the back-pressure was lowered again. At 22.5 bars the pressure drop in the last section of the core (p7-p8) started rising, marking the beginning of degassing of the fluid. The system was then allowed to reach steady state and a scan was taken. In the next step the pressure was lowered again to 20 bars, and again there was a rise in the pressure drop in the last section. In the last step the pressure was lowered to 10 bars, at this moment the section(p6-p7) also degassed and was allowed to reach steady state.

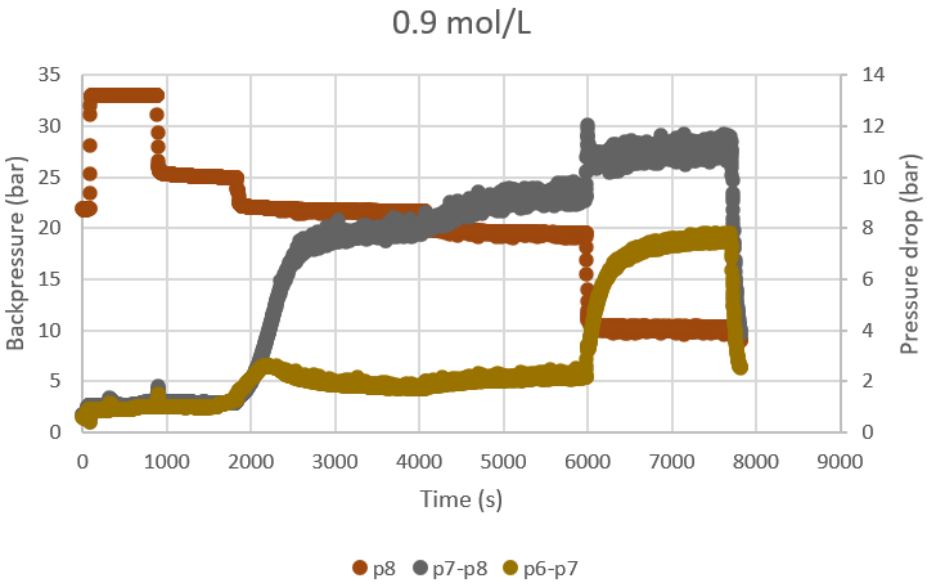

Figure 4.2: Pressure measurements for 0.9 mol/L

The pressure at which degassing is expected is estimated using Henry's law as mention in equation 2.9. The degassing pressure observed for the experiments at different concentrations and the pressures estimated using Henry's Law have been presented in plot 4.3.

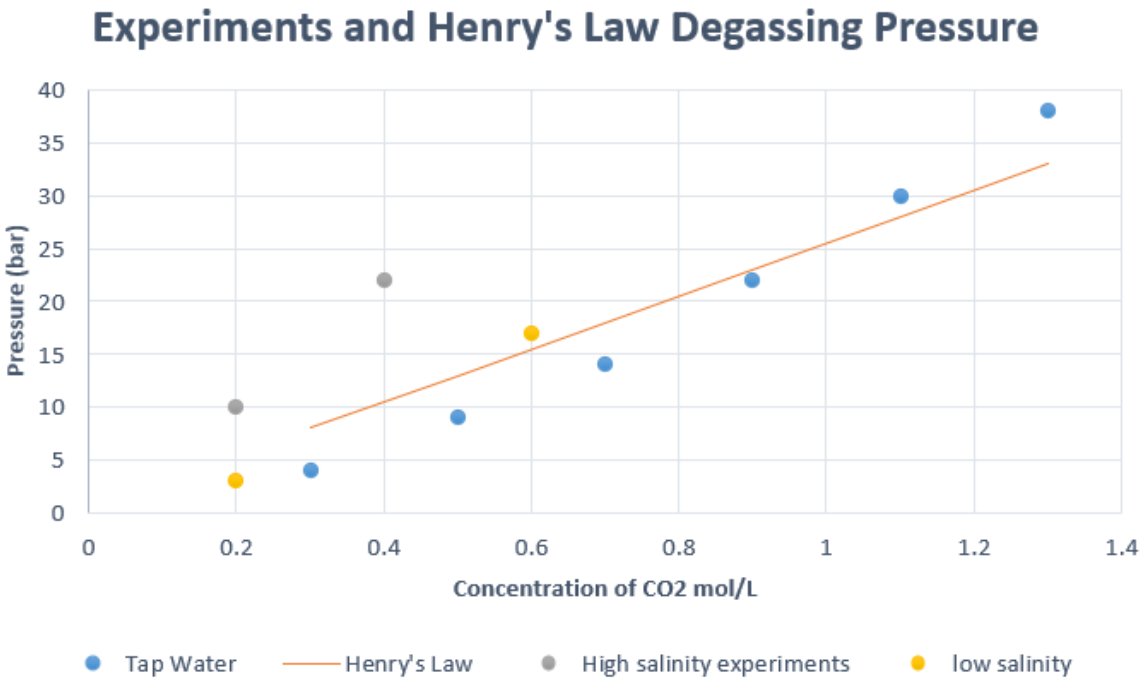

Figure 4.3: Henry's Law and Experiments for degassing pressure

The experiments seem to follow Henry's law but there was an offset of around 4 bars. This offset could be attributed to changing temperature of the CT scan room as it was assumed to be constant (18 ° C). The temperature of the room was observed to be between 17 to 20 ° C. The other reason of the offset could be the concentration of CO_2 being injected in the core. This was controlled by the mass flow controller but usually at concentrations lower than 10 it took a while to get a constant delivery of the flow rate required. At higher concentrations as well the mass flow controller overshoots sometimes and a lot of gas injected in the core which causes an increase in pressure drop over the entire region of the core and then the pressure drop goes back to equilibrium once the gas plug comes out of the core. One of the reasons could also be the reactions between carbon-dioxide and water leading to the formation of carbonic acid. This results in changes of pH of the system and leading to loss of protons. This reaction results in increased solubility of carbon-dioxide which means in order to degas the reaction has to be reversed. Due to this reason at lower system pressures the offset between Henry's law and the experiments is expected to be higher. (Verweij, 2021)

The experiments where brine was used instead of tap water are expected to degas earlier than the expected pressure since with increasing salinity the solubility of gases decreases. When low salinity fluid was injected with a CO_2 concentration of 0.2 mol/L the degassing occurred at lower than expected pressure, however at a concentration of 0.6 mol/L the degassing occurred at higher than expected pressure. When the high salinity brine was used the results were difference between expected and observed degassing was more than 5 bars. The contour plot of iso-solubility lines as a function of temperature and pressure has been presented in Figure 4.4. The low salinity experiments of 0.2 mol/L degassed at the expected pressure of around 5 bars, however 0.6 mol/L degassed at around 17 bars, however according to the model it is expected to degass at around 22 bars.

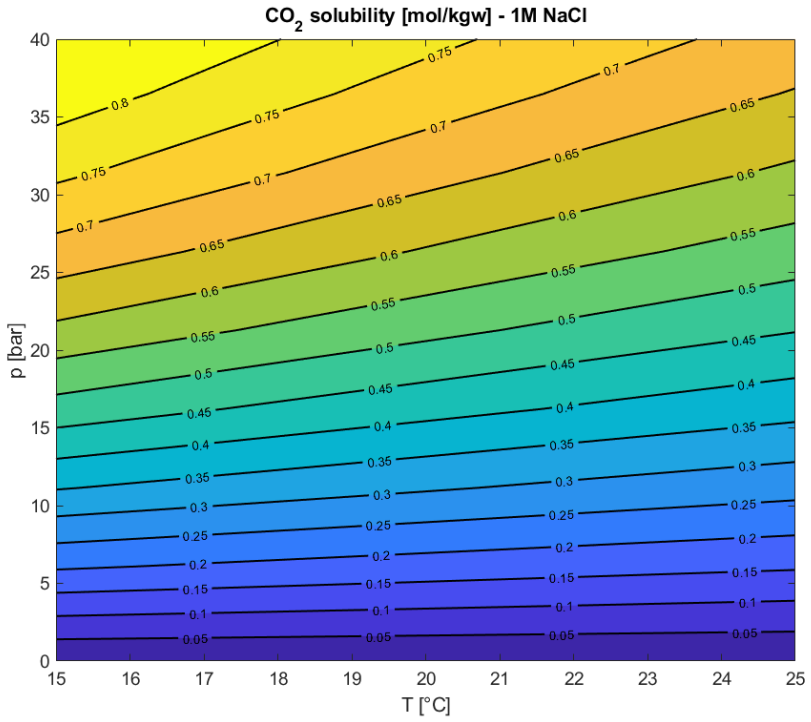

Figure 4.4: Iso-solubility lines for CO_2 as a function of pressure and temperature (Duan & Sun, 2003)

Figure 4.5 presents a plot of effective permeability versus back-pressure for all concentrations of CO_2 injected in experiments. At the start of the experiments it can be observed that the effective permeability is around 0.08 for low concentration experiments and that for higher concentration experiments and low salinity experiments is around 0.06. For high salinity experiments the effective permeability at the start is around 0.02. This means for higher salinity the effective permeability is around four times less. When the degassing process starts the effective permeability decreases to around 0.01. This implies that the effective permeability decreases seven times for lower concentrations and and three times for high salinity experiments.

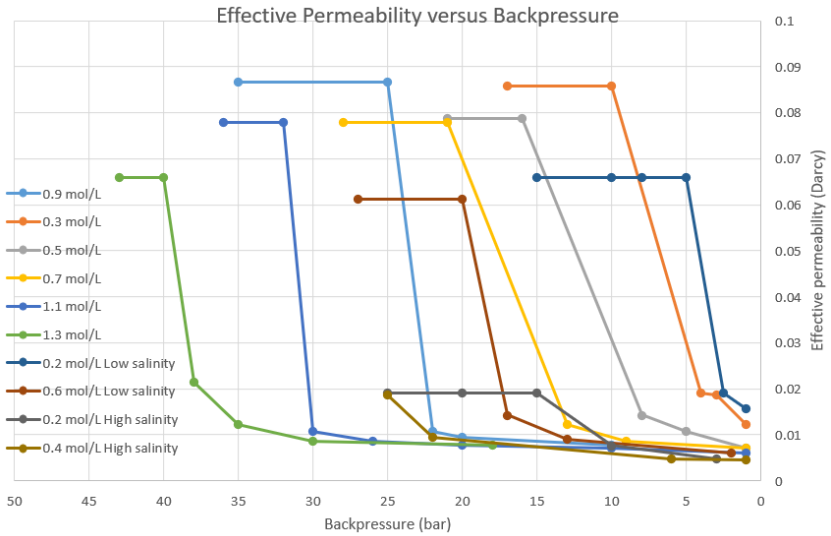

Figure 4.5: Henry's Law and Experiments for degassing pressure

4.3. Porosity Measurement

The porosity map before the start of the core-floods and after the end of all the core-floods have been presented in Figure 4.6, where the plot on the left indicates the porosity values throughout the length of the core at the start and the plot on the right shows the porosity values throughout the length of the core at the end of the core-floods.

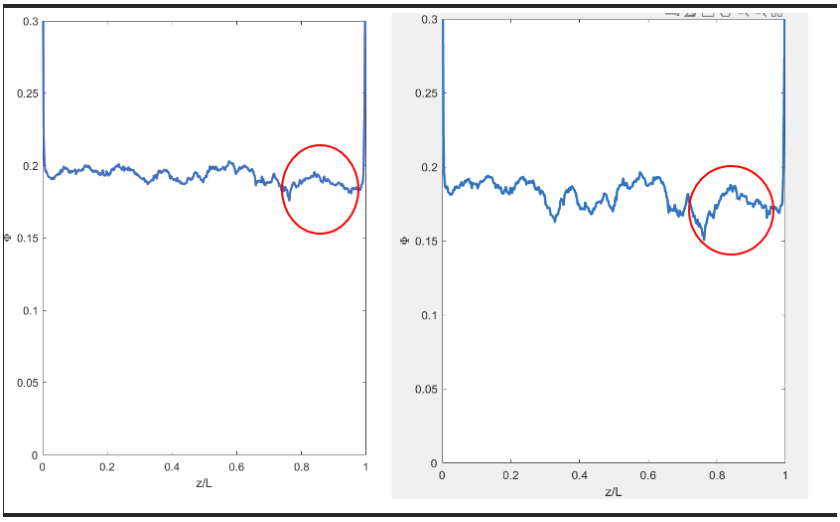

Figure 4.6: (Left) Porosity vs length of core at start (Right) Porosity vs length of core at end

The porosity at the start of the experiment lies between 0.175 to 0.20, and at the end it lies between 0.150 to 0.190. However, the porosity values just after switching tap water with brine are similar to the values at the end of experiment.This indicates a reduction in porosity of the core after after experiments using tap water. This reduction is especially pronounced near the inlet of the core (circled in red). This implies there might have been some blockages at the inlet of the core caused by contaminants in the tap water.

4.4. Saturation Maps

The saturation maps for CO_2 concentration of 0.5 mol/L with a back pressure of 9 bars and 5 bars has been presented in Figure 4.7. The map clearly indicates that as the back-pressure has been lowered the tap water injected has degassed more and the gas front has shifted more from the outlet of the core.

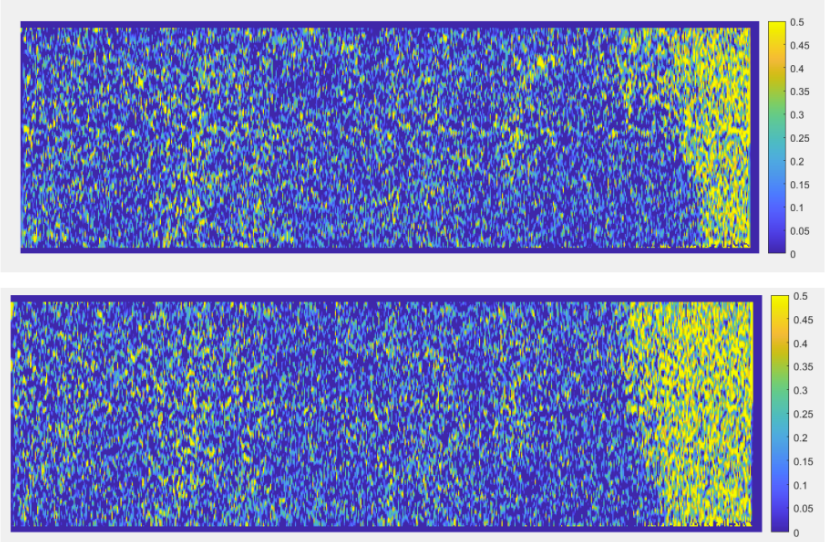

Figure 4.7: (Top)0.5 mol/L at 9 bars(Bottom) 0.5 mol/L at 5 bars

However in higher concentrations of CO_2 the gas front is not clearly observed, rather a gravity effect is occurs. The saturation map for a CO_2 concentration of 0.9 mol/L at a back-pressure of 22 bars and 10 bars have been shown in Figure 4.8 below. Carbon dioxide has a density of 19.28 kg/m^3 at 10 bars and a temperature of 18 ° C, whereas water has a density of 997 kg/m^3. The scans clearly show a gravity segregation effect .In the experiments the injected tap water/brine has a higher density and displaces the less dense bubbles as shown in plot 4.9. (Alamooti & Malekabadi, 2018)

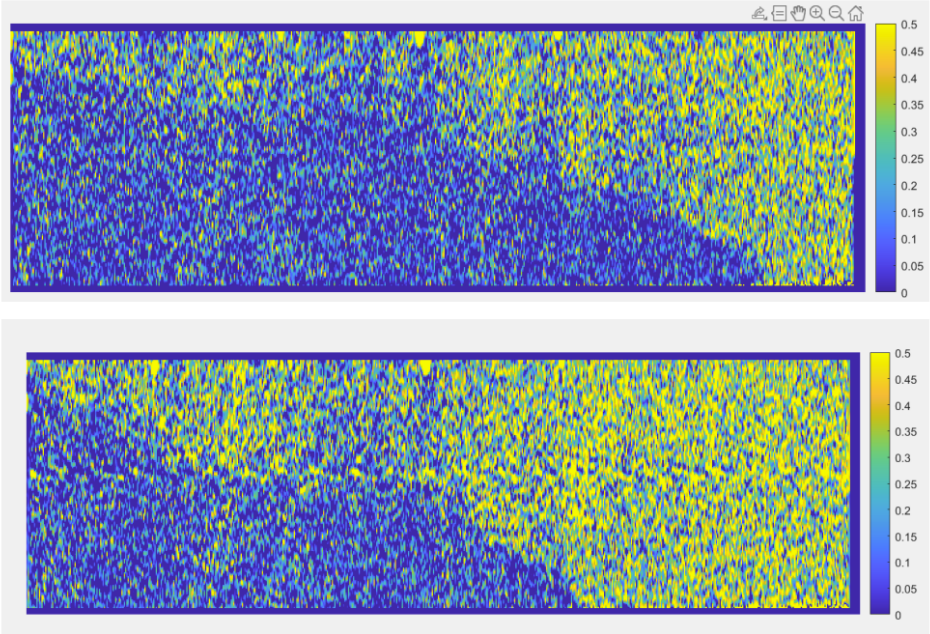

Figure 4.8: (Top)0.9 mol/L at 22 bars(Bottom) 0.9 mol/L at 10 bars

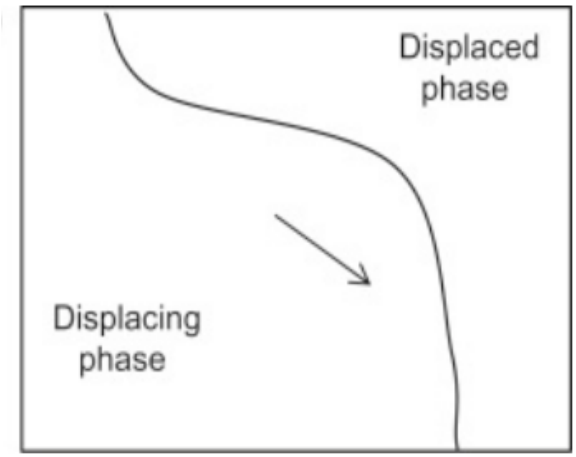

Figure 4.9: Gravity segregation effect observed when the fluid injected is denser (Alamooti & Malekabadi, 2018)

A plot of gas saturation values vs pressure drop at the outlet for different concentrations of CO_2 injected in the core-flood experiments has been shown in Figure 4.11. This plot was made by utilising the saturation values obtained by the saturated scans of the core after degassing. The values in these plots were averaged out by hand and then used to produce the final plot of gas saturation and pressure drop.The saturation values were calculated lower than middle part of the core as shown in Figure 4.10. The values obtained from this method are approximate values.

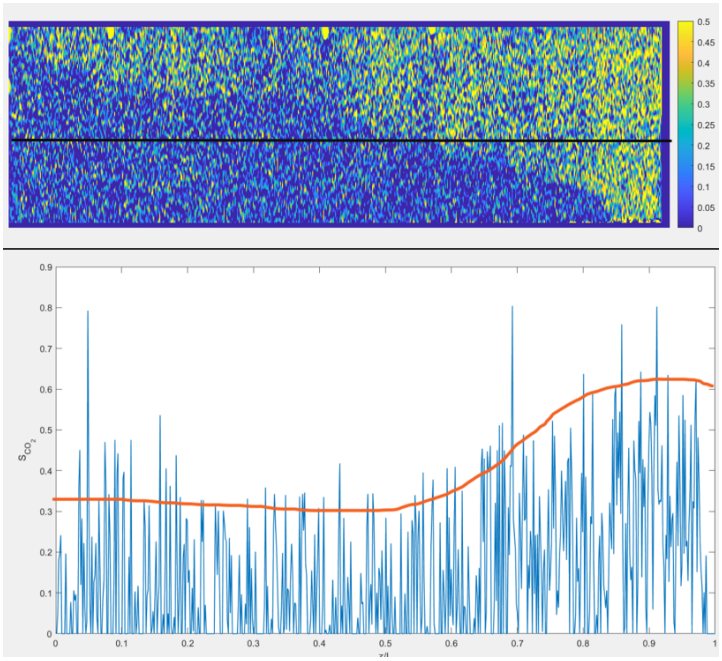

Figure 4.10: Saturation map for 0.9 mol/L, band saturation values taken along the black line with general trend in orange

In general as back pressure is decreased the fluid is degassed. The increase in concentration of bubbles also induces an increase in pressure drop to maintain the flow of fluids and gradually more degassing occurs. The high salinity experiments have been highlighted by the red circle. They experience a higher pressure drop because of the higher concentration of salts dissolved in the fluid. This increases the viscosity of the solution and therefore more drop in pressure is required to maintain the flow at the desired rate.

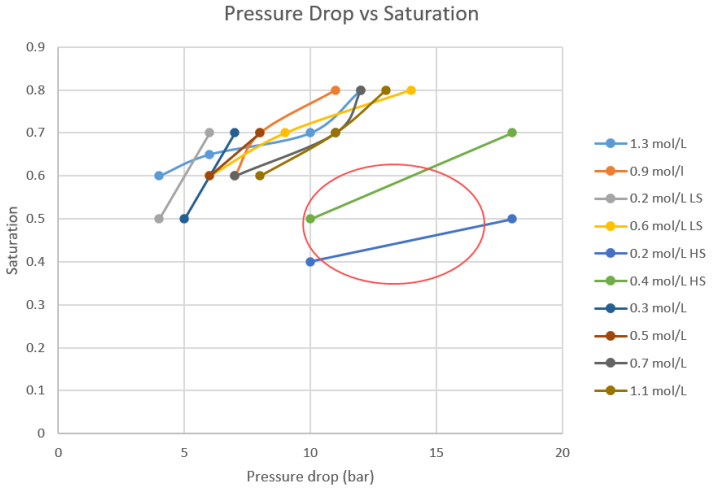

Figure 4.11: Pressure drop vs saturation of gas at different concentrations of CO_2, red circle highlights HS experiments

5

Conclusion

The aim of this research project was to visualise degassing of geothermal fluids by the use of CT assisted core-flood experiments. This was also accompanied by permeability and porosity calculations before the start of experiments, then once after changing to brine and finally at the end of the experiments in order to understand the changes that occurred in the core in the duration of the experimental research. The permeability over the whole core decreased by a factor of 2 after the end of experiments potentially due to the usage of high salinity brine resulting in calcite precipitation. Similarly the outlet of the core also experienced a decrease in permeability by a factor of 3. The expected degassing pressure of the brine or tap water being used was estimated by using Henry's Law. The experiments follow the curve of Henry's Law at 18° C with an offset of around 4 bars. This could be due to the variations in room temperature, the changes in pH and subsequent formation of carbonic acid and maybe due to the mass flow controller overshooting sometimes. For the low salinity experiments a model by Duan and Sun was used to construct a contour plot of solubility as a function of temperature and pressure. The 0.2 mol/L experiment follows the model. A plot of effective permeability versus pressure drop indicated that higher salinity experiments had an initial effective permeability four times less than low concentration experiments. The porosity was calculated using dry scan and wet scans before the experiments, after switching with brine and at the end of the experiments. They also show a decrease in porosity values after the switching with brine and more significantly at the inlet. Finally, saturation maps and plots were created to visualise the degassing of the fluids inside the core. At low concentrations of CO_2 a definite gas front is observed as the degassing proceeds with decreasing back pressure. On the other hand, at higher CO_2 concentration the "gravity segregation effect" is observed due to the difference in density of gas and the water or brine flowing. A plot of saturation values versus pressure drop was made to summarise the gas concentrations at various pressure drops for different experiments. The plot reflected that the high salinity experiments involve greater pressure drops in order to maintain the flow rates.

5.1. Recommendations

This section provides a list of recommendations for upcoming research on degassing of geothermal fluids

- One of the areas of uncertainty for the experiments were variations in temperature. A more definite control in temperature for future experiments would allow a much better comparison with existing laws to estimate degassing pressures.
- The CT assisted core-floods were carried out in temperatures of around 18° C. It would be useful to obtain saturation maps for higher temperatures since they would be closer to subsurface conditions.
- The model using equation of Duan and Sun was used to compare the results from low salinity brine. However, it would be useful to obtain a model to compare the results of high salinity brine as well.

- There was already a decrease in porosity and permeability just after switching tap water with brine. This was thought to be due to contaminants present in tap water that might have blocked the inlet. In future experiments this could be researched more extensively to verify the explanation.
- The core-floods were carried out at a set flow rate of 15ml/min and at different concentration of CO_2. In future research different flow rates with the same concentration and temperature could be used to obtain saturation maps and visualise how it impacts the flow of gas.
- A Berea core was used for the core-floods and was assumed to have uniform permeability throughout the core. For future experiments the permeability variations throughout the core can be obtained and then its implications for the obtained saturation maps and values can be studied.

Bibliography

References

Alamooti, A. M., & Malekabadi, F. K. (2018). Chapter one - an introduction to enhanced oil recovery. In A. Bahadori (Ed.), *Fundamentals of enhanced oil and gas recovery from conventional and unconventional reservoirs* (p. 1-40). Gulf Professional Publishing. Retrieved from https://www.sciencedirect.com/science/article/pii/B9780128130278000011 doi: https://doi.org/10.1016/B978-0-12-813027-8.00001-1

Atangana, A. (2018). Chapter 2 - principle of groundwater flow. In A. Atangana (Ed.), *Fractional operators with constant and variable order with application to geo-hydrology* (p. 15-47). Academic Press. Retrieved from https://www.sciencedirect.com/science/article/pii/B9780128096703000023 doi: https://doi.org/10.1016/B978-0-12-809670-3.00002-3

Benson, S. M., Perrin, J.-C., Krause, M., Kuo, C.-W., & Miljković, L. (2008). Experimental investigations of multiphase flow and trapping in saline aquifers - annual report 2007 -..

Blöcher, G., Reinsch, T., Henninges, J., Milsch, H., Regenspurg, S., Kummerow, J., ... Huenges, E. (2016). Hydraulic history and current state of the deep geothermal reservoir groß schönebeck. *Geothermics*, *63*, 27-43. Retrieved from https://www.sciencedirect.com/science/article/pii/S0375650515000917 (Enhanced Geothermal Systems: State of the Art) doi: https://doi.org/10.1016/j.geothermics.2015.07.008

Chabab, S., Cruz, J. L., Poulain, M., Ducousso, M., Contamine, F., Serin, J. P., & Cézac, P. (2021). Thermodynamic modeling of mutual solubilities in gas-laden brines systems containing co2, ch4, n2, o2, h2, h2o, nacl, cacl2, and kcl: Application to degassing in geothermal processes. *Energies*, *14*(17). Retrieved from https://www.mdpi.com/1996-1073/14/17/5239 doi: 10.3390/en14175239

Dawson, G., Pearce, J., Biddle, D., & Golding, S. (2015). Experimental mineral dissolution in berea sandstone reacted with co2 or so2–co2 in nacl brine under co2 sequestration conditions. *Chemical Geology*, *399*, 87-97. Retrieved from https://www.sciencedirect.com/science/article/pii/S0009254114004446 (Measuring and predicting the geochemical impacts of CO2 storage on reservoir rocks) doi: https://doi.org/10.1016/j.chemgeo.2014.10.005

Duan, Z., & Sun, R. (2003). An improved model calculating co2 solubility in pure water and aqueous nacl solutions from 273 to 533 k and from 0 to 2000 bar. *Chemical Geology*, *193*(3), 257-271. Retrieved from https://www.sciencedirect.com/science/article/pii/S0009254102002632 doi: https://doi.org/10.1016/S0009-2541(02)00263-2

EBN , DAGO, Mckinsey Company, & Stichting Platform Geothermie. (2019, 01). *Masterplan Geothermal Energy in the Netherlands* (Tech. Rep.). Retrieved from https://geothermie.nl/images/bestanden/Masterplan_Aardwarmte_in_Nederland_ENG.pdf

Finster, M., Clark, C., Schroeder, J., & Martino, L. (2015). Geothermal produced fluids: Characteristics, treatment technologies, and management options. *Renewable and Sustainable Energy Reviews*, *50*, 952-966. Retrieved from https://www.sciencedirect.com/science/article/pii/S1364032115005298 doi: https://doi.org/10.1016/j.rser.2015.05.059

Fitts, C. R. (2013). 2 - physical properties. In C. R. Fitts (Ed.), *Groundwater science (second edition)* (Second Edition ed., p. 23-45). Boston: Academic Press. Retrieved from https://www.sciencedirect.com/science/article/pii/B9780123847058000029 doi: https://doi.org/10.1016/B978-0-12-384705-8.00002-9

Flores, J., Meza, O., L., S., & Aragón, A. (2017). The effect of salinity and gas saturation of a geothermal fluid on the reservoir permeability reduction. *Geofísica Internacional*, *56*(4). doi: 10.22201/igeof.00167169p.2017.56.4.1826

Gielen, D., Boshell, F., Saygin, D., Bazilian, M. D., Wagner, N., & Gorini, R. (2019). The role of renewable energy in the global energy transformation. *Energy Strategy Reviews*, *24*, 38-50. Retrieved from https://www.sciencedirect.com/science/article/pii/S2211467X19300082 doi: https://doi.org/10.1016/j.esr.2019.01.006

Haizlip, J., Stover, M., Garg, S., Tut Haklidir, F., & Prina, N. (2016, 02). Origin and impacts of high concentrations of carbon dioxide in geothermal fluids of western turkey..

Hermann, C., Dewes, I., & Schumpe, A. (1995). The estimation of gas solubilities in salt solutions. *Chemical Engineering Science*, *50*(10), 1673-1675. Retrieved from https://www.sciencedirect.com/science/article/pii/000925099500031Y doi: https://doi.org/10.1016/0009-2509(95)00031-Y

IRENA . (2022, 03). *World Energy Transitions Outlook: 1.5°C Pathway* (Tech. Rep.). Retrieved from https://www.irena.org/publications/2022/Mar/World-Energy-Transitions-Outlook-2022

Lev, M., & Gonzalez, R. (2002). 17 - ct angiography and ct perfusion imaging. In A. W. Toga & J. C. Mazziotta (Eds.), *Brain mapping: The methods (second edition)* (Second Edition ed., p. 427-484). San Diego: Academic Press. Retrieved from https://www.sciencedirect.com/science/article/pii/B9780126930191500198 doi: https://doi.org/10.1016/B978-012693019-1/50019-8

Mahabadi, N., Zheng, X., Yun, T. S., van Paassen, L., & Jang, J. (2018). Gas Bubble Migration and Trapping in Porous Media: Pore-Scale Simulation. *Journal of Geophysical Research: Solid Earth*, *123*(2), 1060–1071. doi: 10.1002/2017jb015331

Ornelas, O. (2012, December). *Salton sea could get new geothermal power plant.* https://eu.desertsun.com/story/tech/science/energy/2016/03/15/salton-sea-could-get-new-geothermal-power-plant/81839422/.

Pepper, J. F., de Witt, W., & Demarest, D. F. (1954). Geology of the Bedford Shale and Berea Sandstone in the Appalachian Basin. *Science*, *119*(3094), 512–513. doi: 10.1126/science.119.3094.512.b

Sander, R. (2015). Compilation of henry's law constants (version 4.0) for water as solvent. *Atmospheric Chemistry and Physics*, *15*(8), 4399–4981. Retrieved from https://acp.copernicus.org/articles/15/4399/2015/ doi: 10.5194/acp-15-4399-2015

Verweij, C. (2021). *CO2 degassing of geothermal fluids during coreflood experiments* (Tech. Rep. No. Master's Thesis).

Wang, L., Li, Y.-L., Zhao, G., Chen, N., & Xu, Y. (2019, 11). Experimental investigation of flow characteristics in porous media at low reynolds numbers (re→0) under different constant hydraulic heads. *Water*, *11*, 2317. doi: 10.3390/w11112317

Wetzel, M., Kempka, T., & Kühn, M. (2021, 01). Diagenetic trends of synthetic reservoir sandstone properties assessed by digital rock physics. *Minerals*, *11*, 151. doi: 10.3390/min11020151

Wildenschild, D., Armstrong, R. T., Herring, A. L., Young, I. M., & William Carey, J. (2011). Exploring capillary trapping efficiency as a function of interfacial tension, viscosity, and flow rate. *Energy Procedia*, *4*, 4945-4952. Retrieved from https://www.sciencedirect.com/science/article/pii/S1876610211007430 (10th International Conference on Greenhouse Gas Control Technologies) doi: https://doi.org/10.1016/j.egypro.2011.02.464

Zuo, L., & Benson, S. M. (2014). Co2 exsolution – challenges and opportunities in subsurface flow management. *Energy Procedia*, *63*, 5664-5670. Retrieved from https://www.sciencedirect.com/science/article/pii/S187661021402414X (12th International Conference on Greenhouse Gas Control Technologies, GHGT-12) doi: https://doi.org/10.1016/j.egypro.2014.11.599

A

Results of the experiments

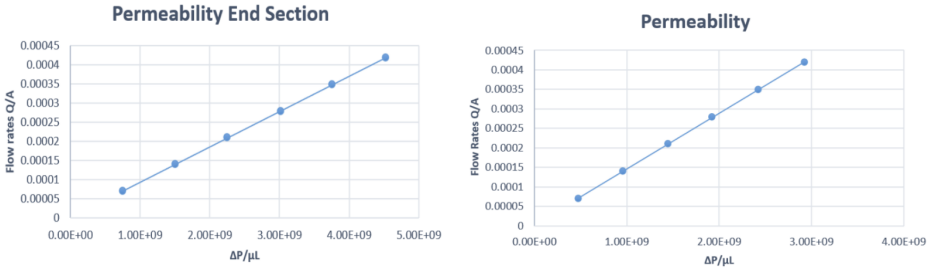

Figure A.1: Permeability at start for overall and end section

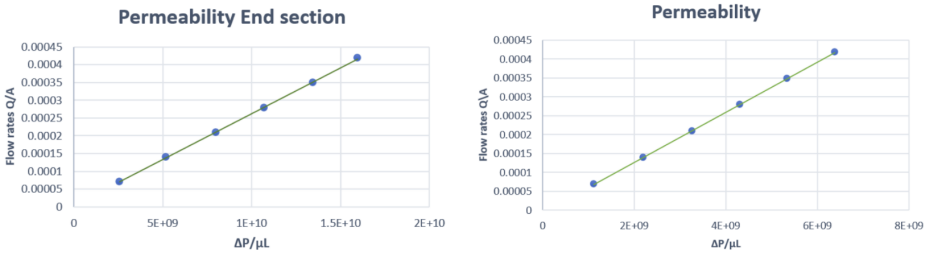

Figure A.2: Permeability at end of experiments for overall and end section

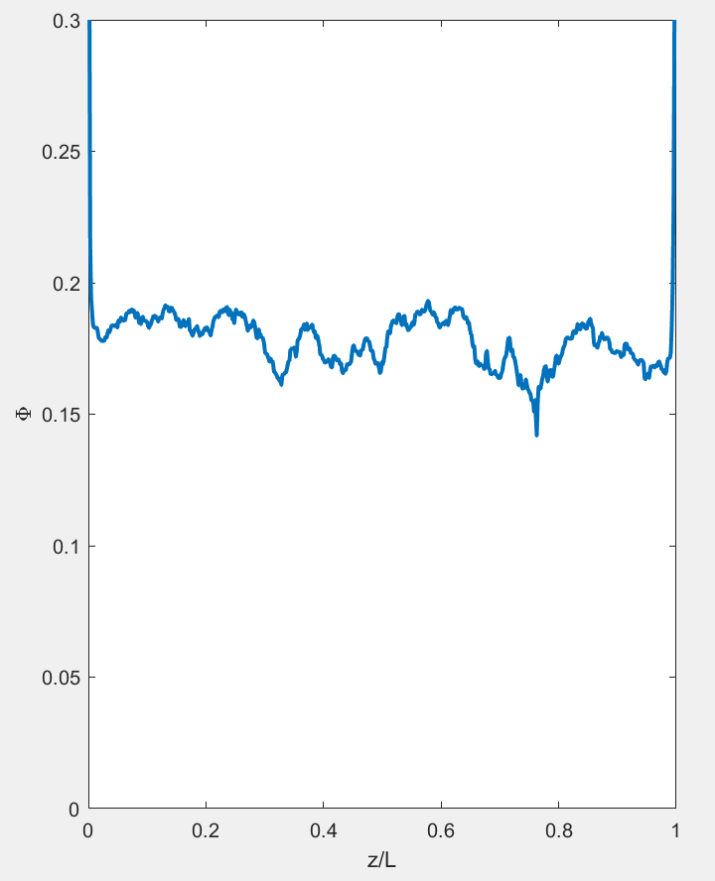

Figure A.3: Porosity map after switching tap water with brine

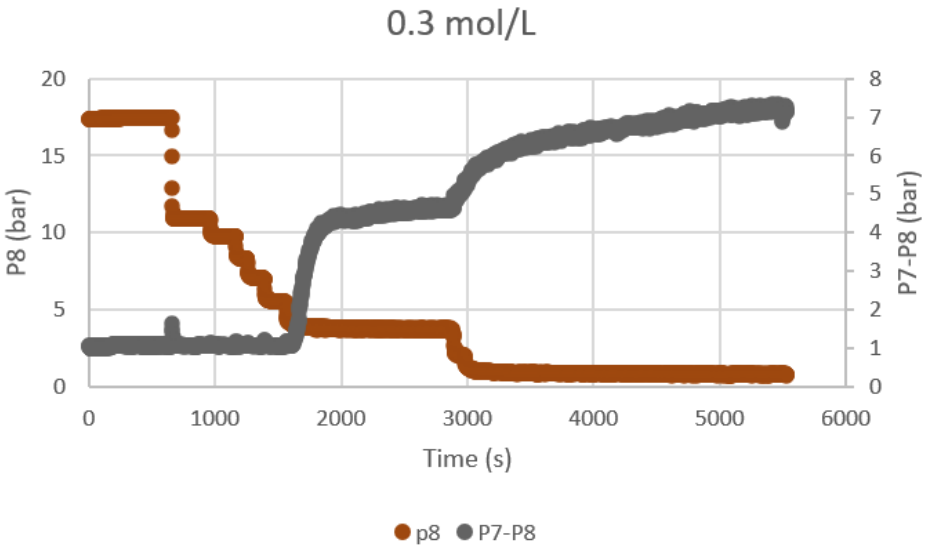

Figure A.4: Pressure measurements 0.3 mol/L

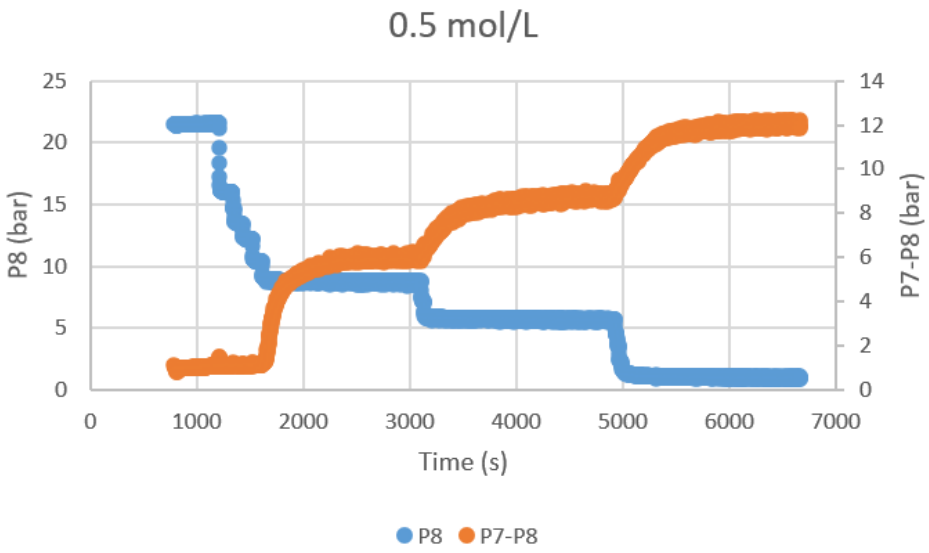

Figure A.5: Pressure measurements 0.5 mol/L

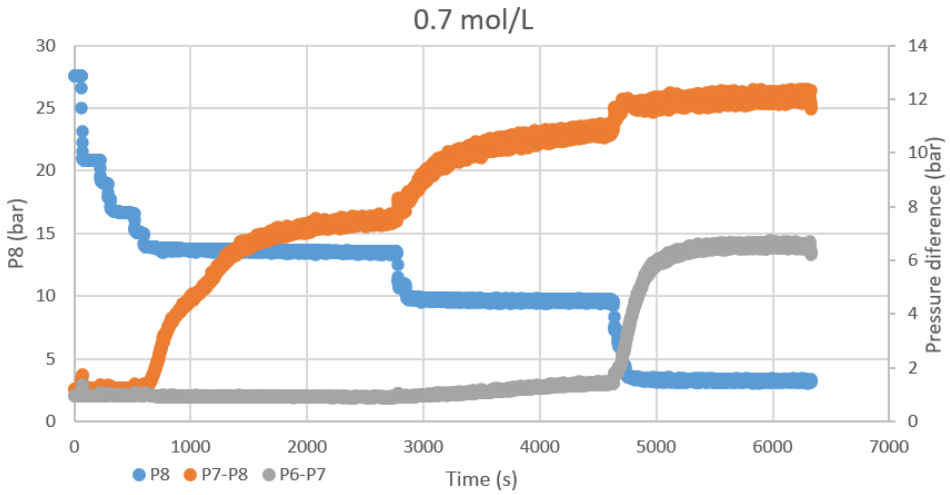

Figure A.6: Pressure measurements 0.7 mol/L

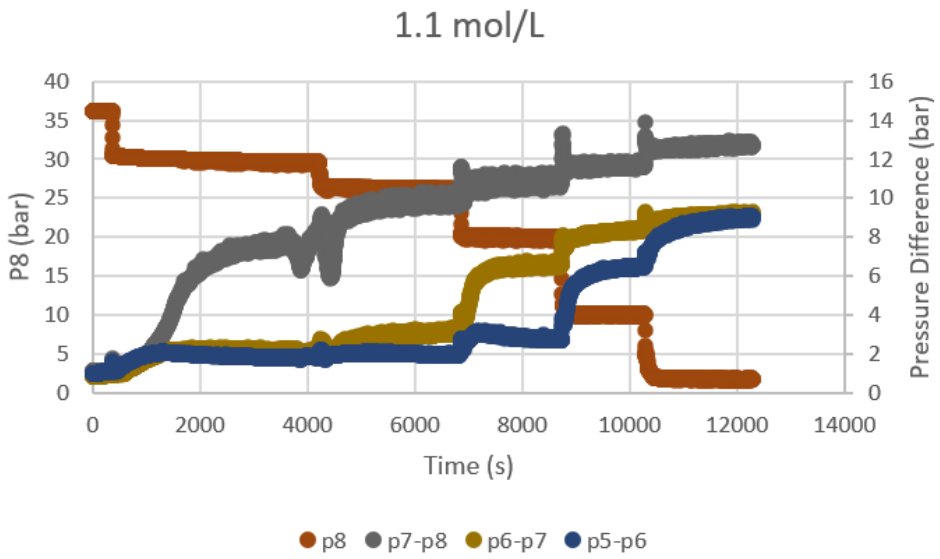

Figure A.7: Pressure measurements 1.1 mol/L

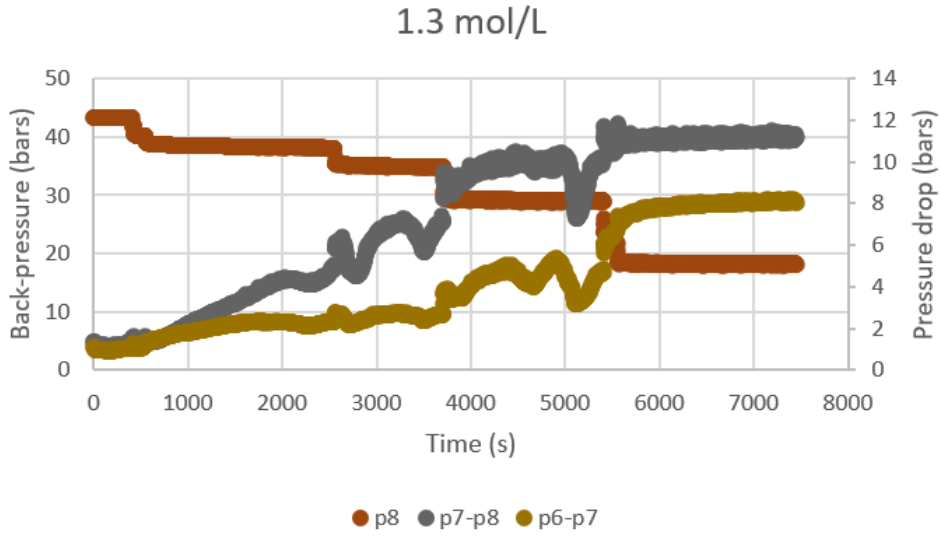

Figure A.8: Pressure measurements 1.3 mol/L

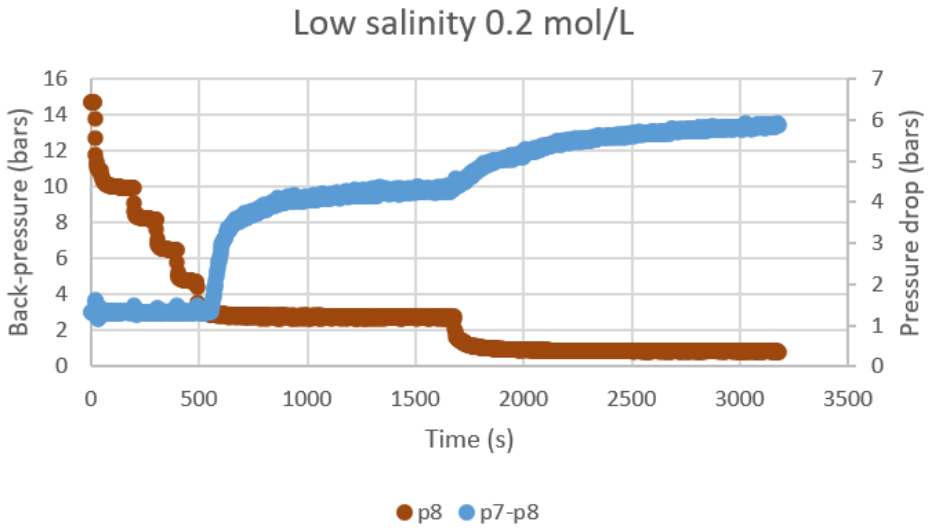

Figure A.9: Pressure measurements 0.2 mol/L low salinity

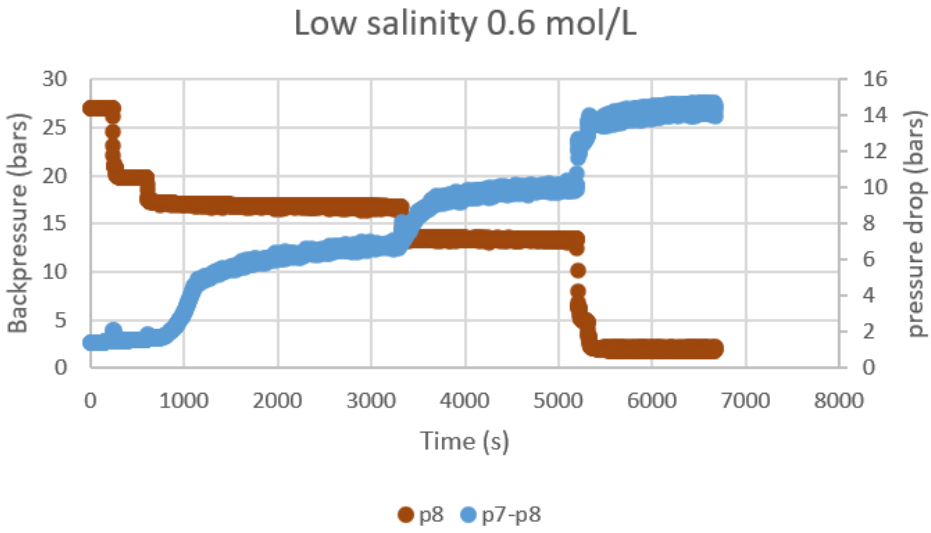

Figure A.10: Pressure measurements 0.6 mol/L Low salinity

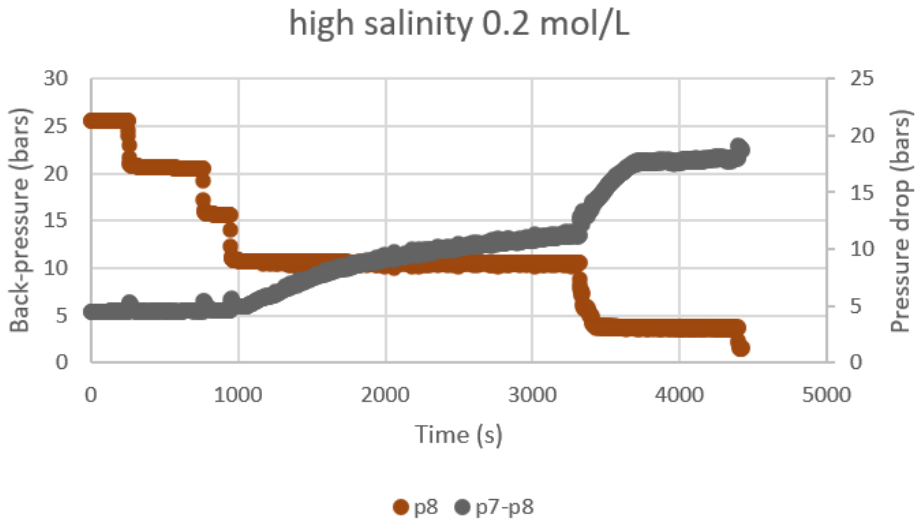

Figure A.11: Pressure measurements 0.2 mol/L high salinity

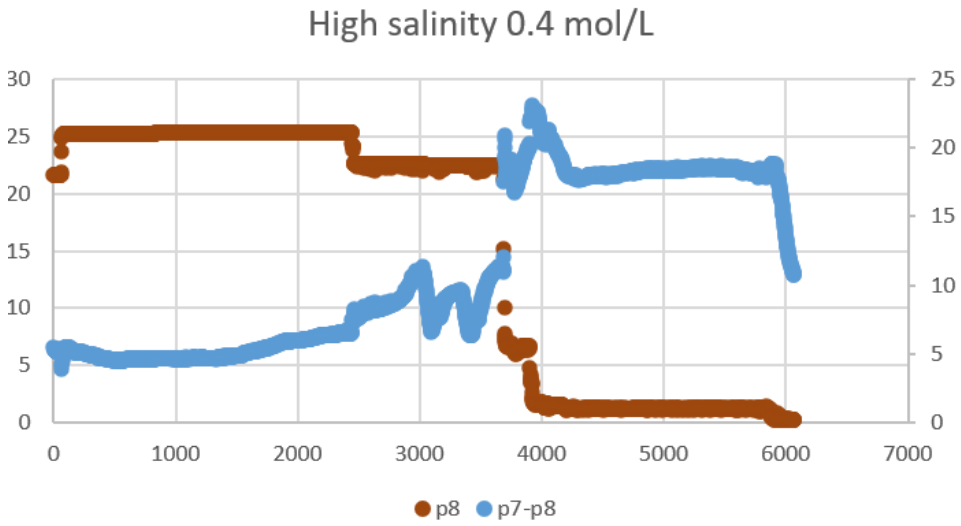

Figure A.12: Pressure measurements 0.4 mol/L High salinity

1.3 mol/L

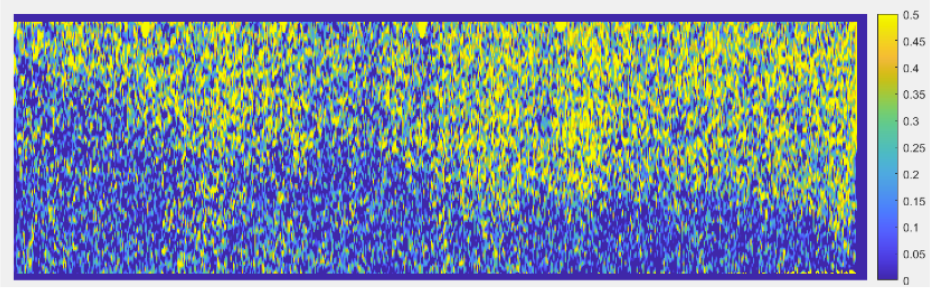

38 bars

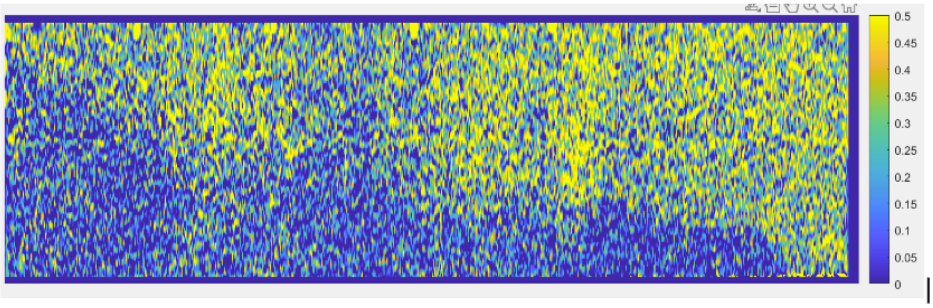

35 bars

Figure A.13

1.3 mol/L

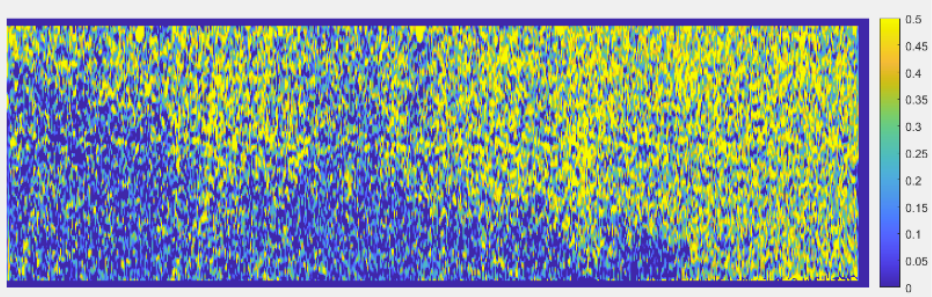

29 bars

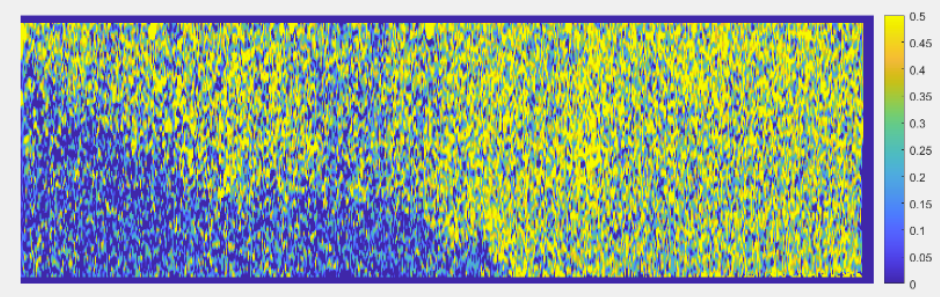

18 bars

Figure A.14

1.1 mol/L

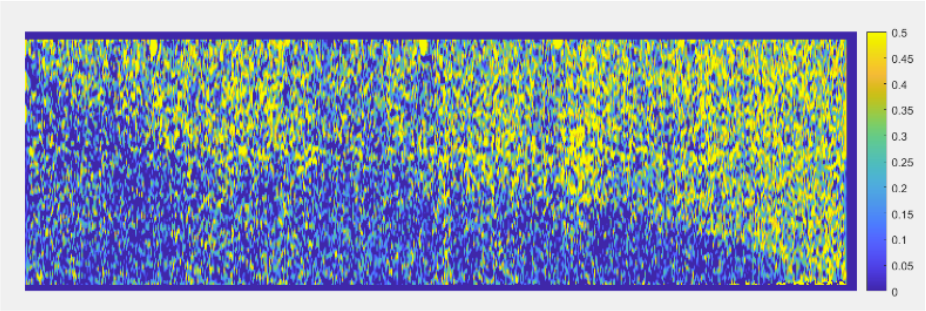

30 bars

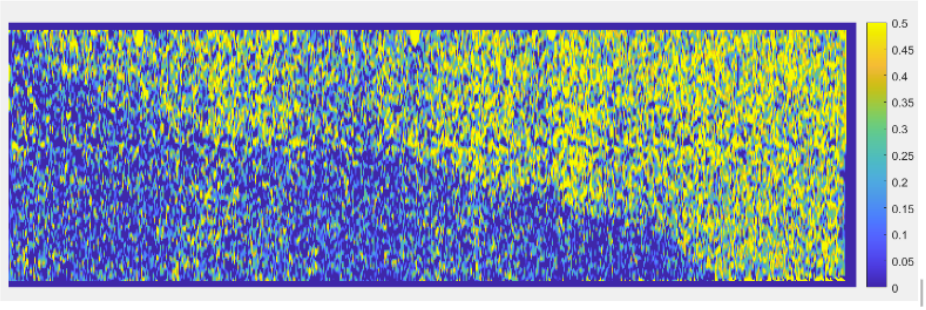

26 bars

Figure A.15

1.1 mol/L

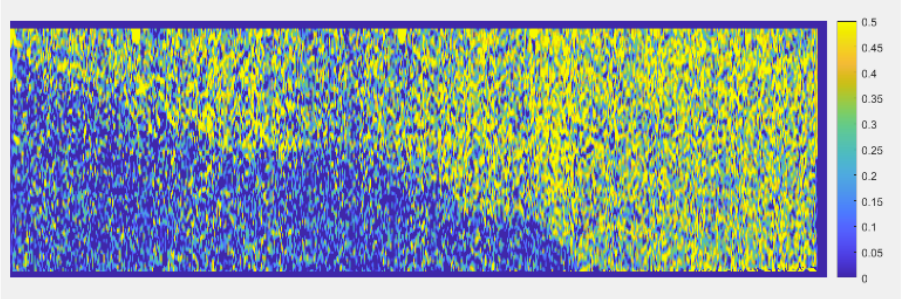

20 bars

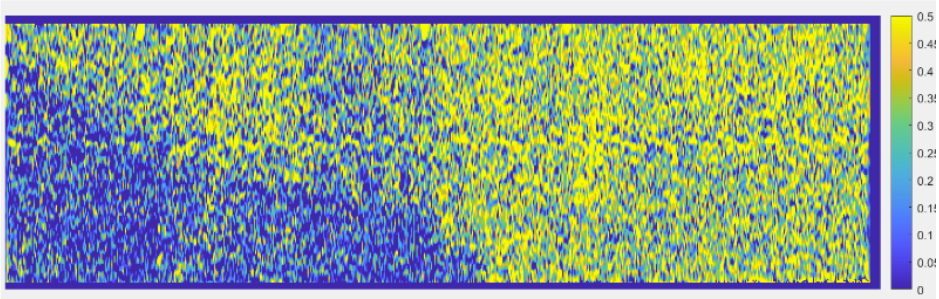

10 bars

Figure A.16

0.9 mol/L

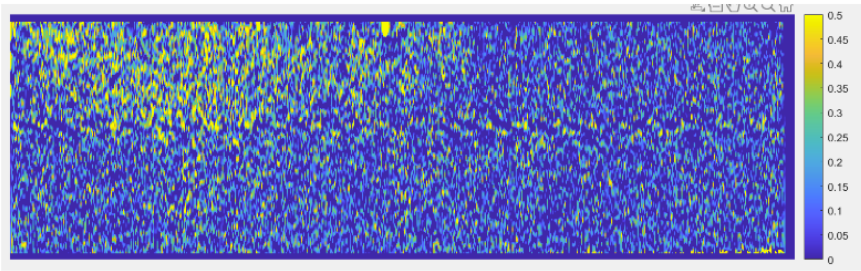

25 bars

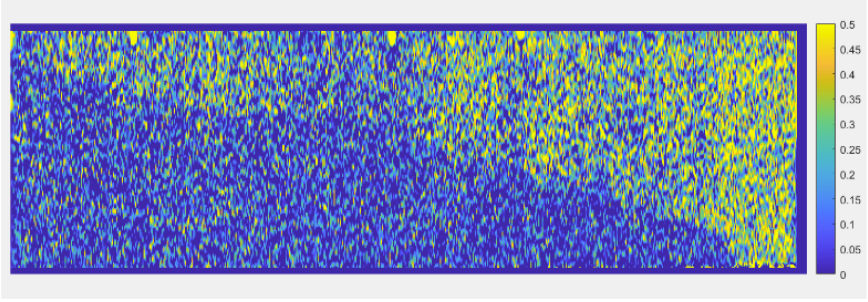

23 bars

Figure A.17

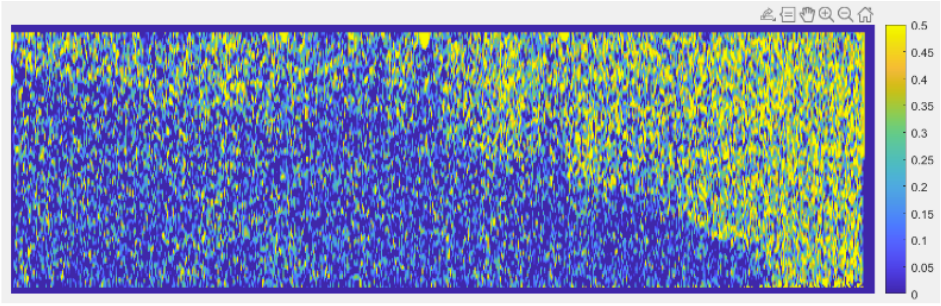

22 bars

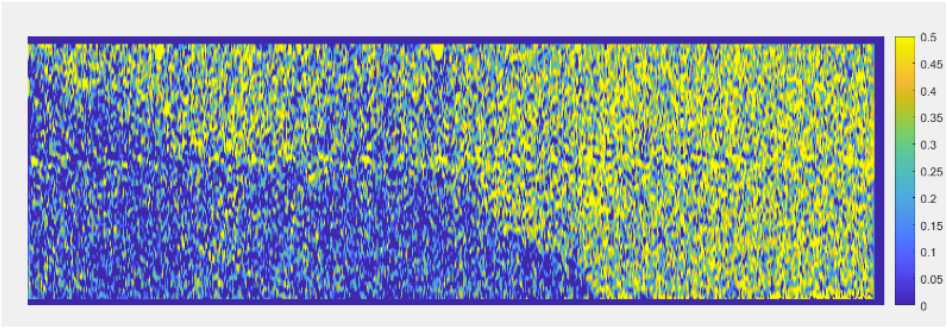

10 bars

Figure A.18

0.7 mol/L

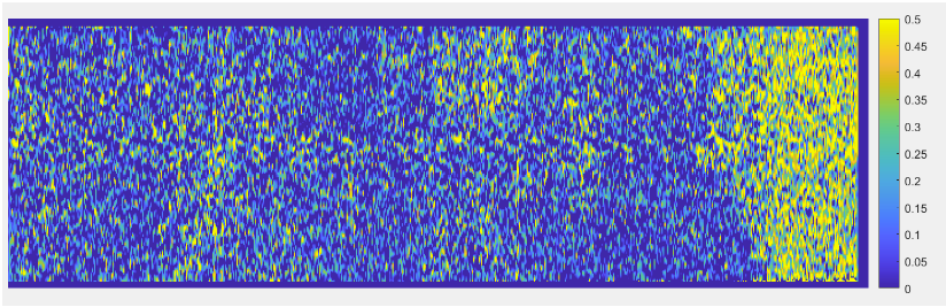

14 bars

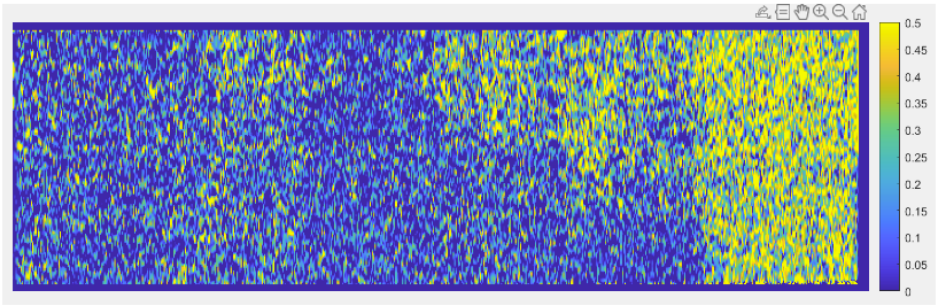

10 bars

Figure A.19

0.7 mol/L

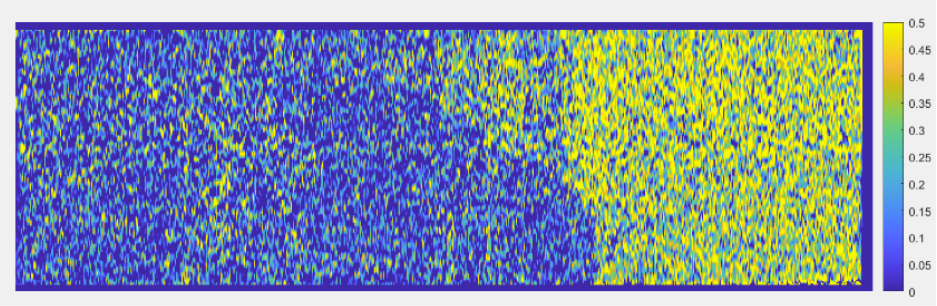

3 bars

Figure A.20

0.5 mol/L

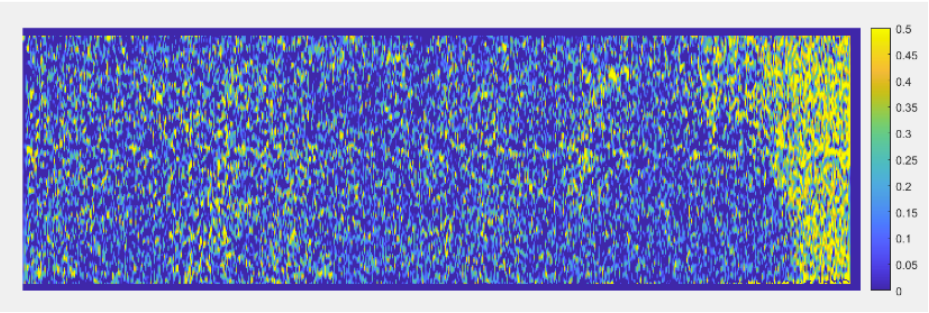

9 bars

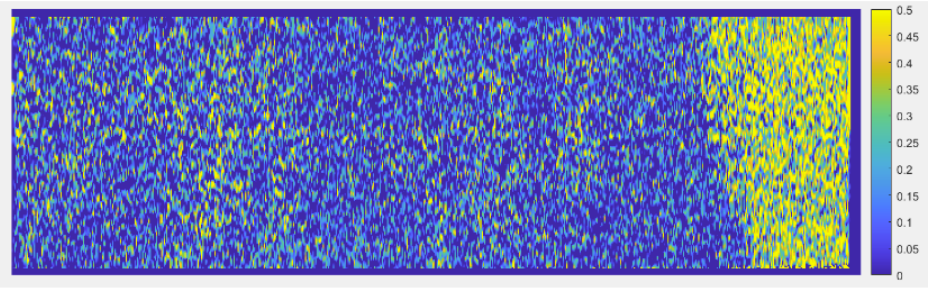

5 bars

Figure A.21

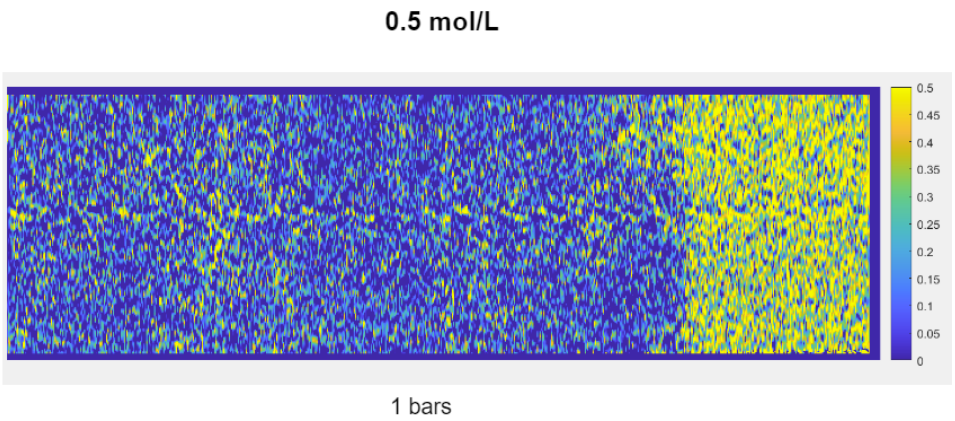

Figure A.22

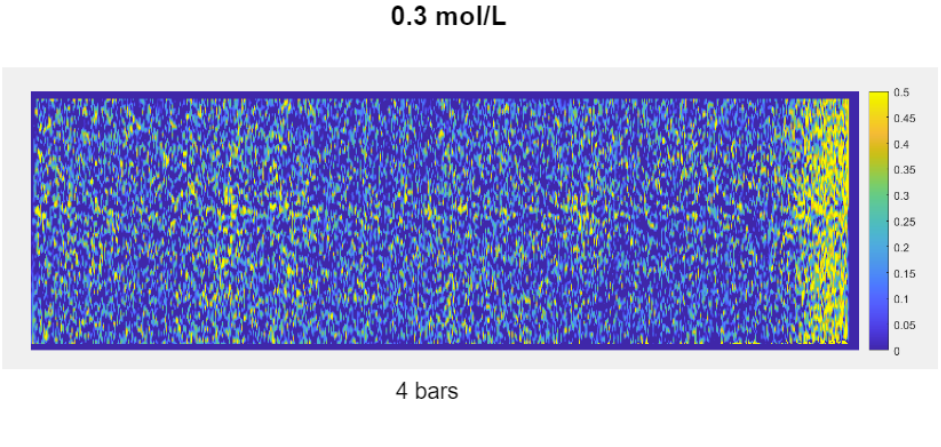

Figure A.23

0.2 mol/L Low salinity

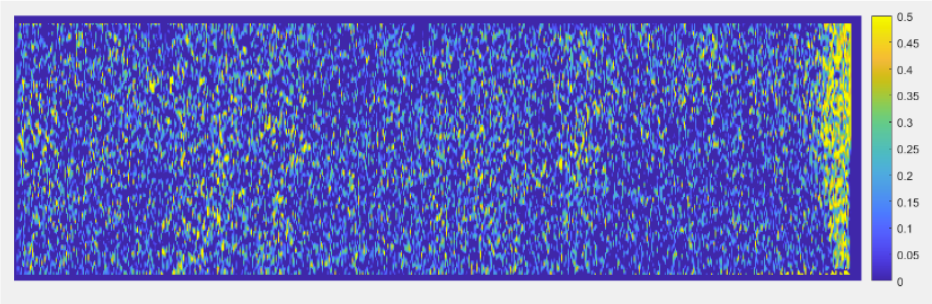

3 bars

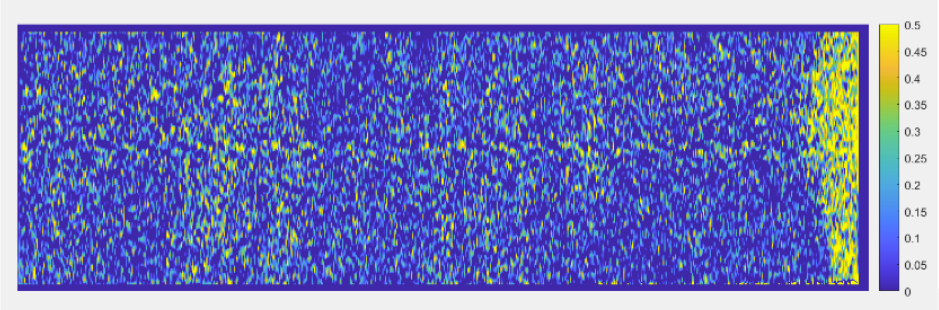

1 bar

Figure A.24

0.6 mol/L Low salinity

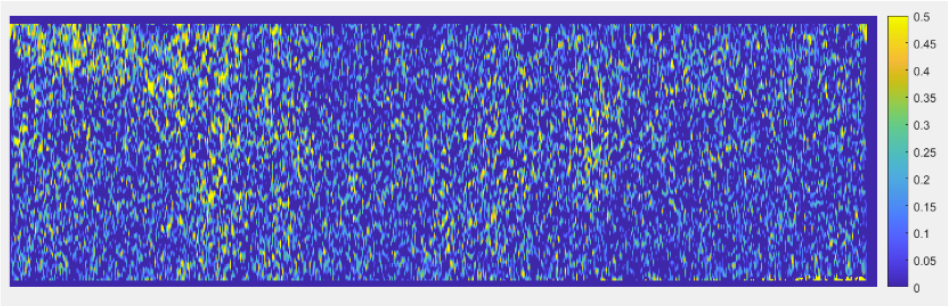

20 bars

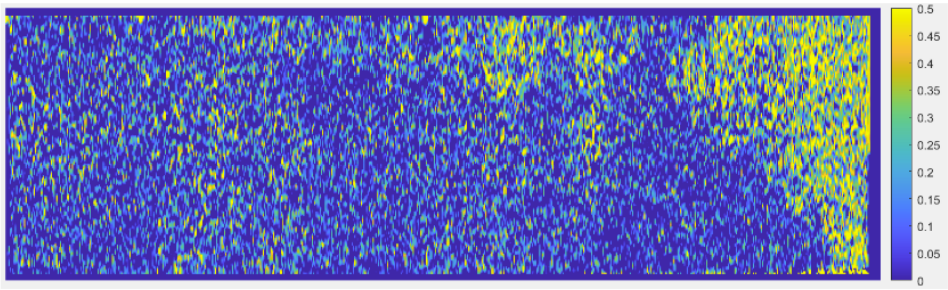

17 bars

Figure A.25

0.6 mol/L Low salinity

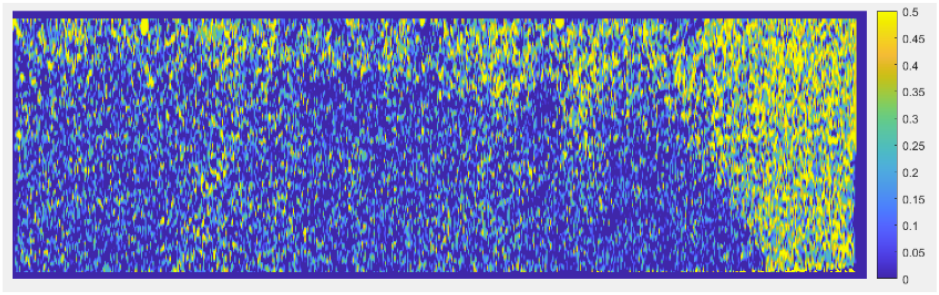

14 bars

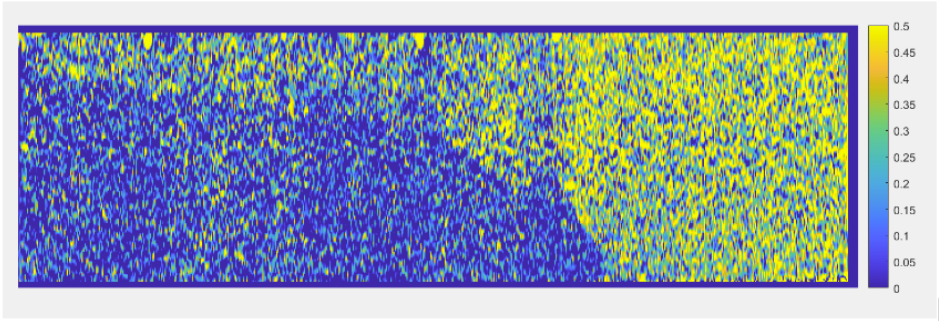

2 bars

Figure A.26

0.2 mol/L High salinity

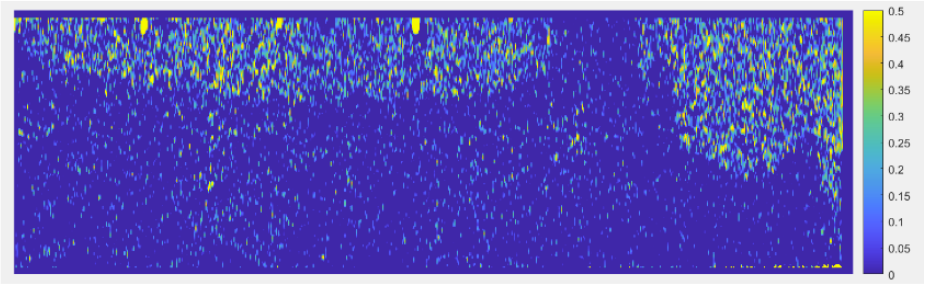

10 bars

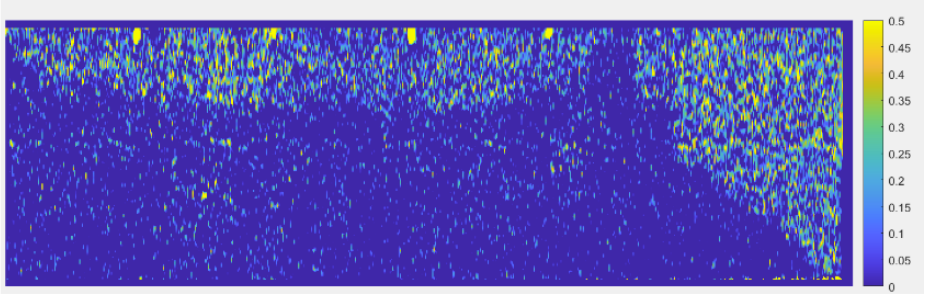

4 bars

Figure A.27

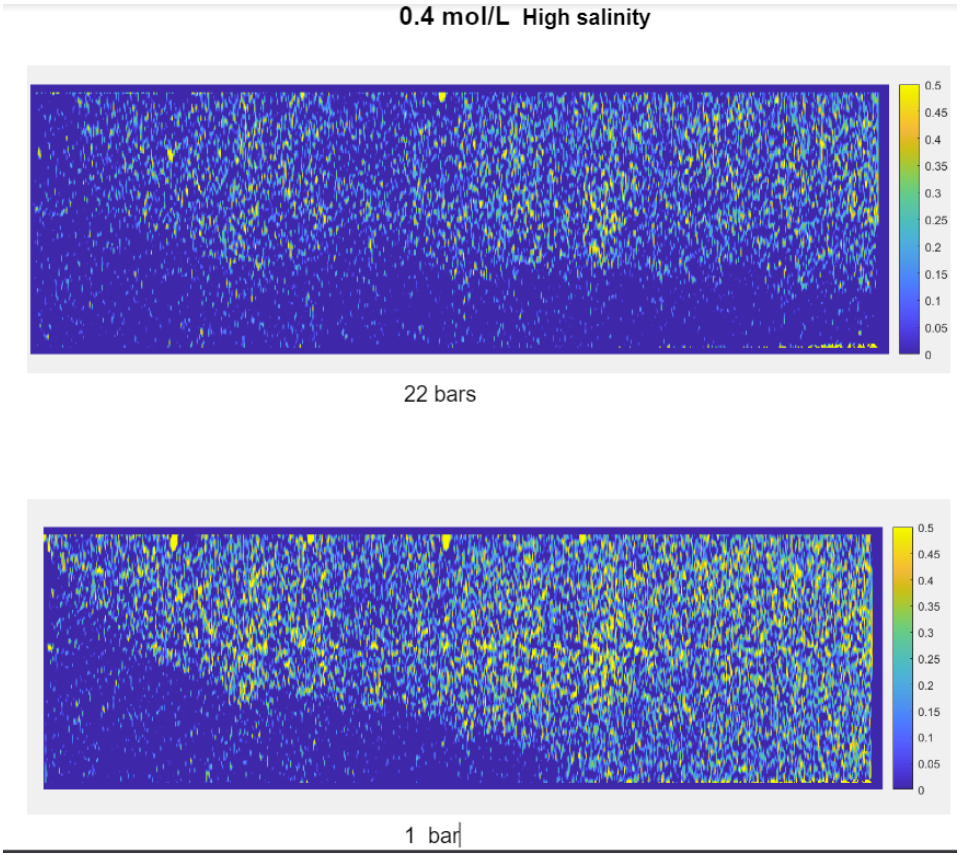
0.4 mol/L High salinity
0.5
0.45
0.4
0.35
0.3
0.25
0.2
0.15
0.1
0.05
0
22 bars
0.5
0.45
0.4
0.35
0.3
0.25
0.2
0.15
0.1
0.05
0
1 bar

Figure A.28